

**REALIZATION OF CMOS COMPATIBLE MICROMACHINED CHEMICAL
SENSORS**

by
TUĞBA DEMİRCİ

Submitted to the Graduate School of Engineering and Natural Sciences
in partial fulfillment of
the requirements for the degree of
Master of Science

Sabancı University

Spring 2002

REALIZATION OF CMOS COMPATIBLE MICROMACHINED CHEMICAL SENSORS

APPROVED BY

Assist. Prof. Dr. Yaşar GÜRBÜZ
(Thesis Supervisor)

Assist. Prof. Dr. Ayhan BOZKURT

Assist. Prof. Dr. Mehmet KESKİNÖZ

DATE OF APPROVAL:

©Tuğba Demirci 2002

All Rights Reserved

to my parents

&

my brothers

ACKNOWLEDGMENTS

There are some people, without whom this thesis would not have come to existence.

First, I would like to express my endless appreciation to my advisor Yaşar Gürbüz. I am grateful for his patient guidance, support and encouragement in all aspects of this work. I would like to thank Ayhan Bozkurt for his help especially with the learning and using ANSYS for the simulations of the design.

Then, I would like to thank Prof. Yusuf Leblebici for his valuable guidance and support.

Furthermore, I would like to thank Ayça Çesmelioglu, Beril Çiftçi, Emrah Üstünay, Gamze Yurttutan, Özhan Öztürk, Mansoor Naseer, Mustafa Parlak, Müge Şahin and Sanem Kabadayı for their friendship and making my life at Sabancı University colorful. I also wish to thank our master Bülent Köroğlu (Bülent Abi) for his precious help.

Lastly, I would like to thank my parents for everything they give me and provide especially during my 18-year-school life. Without them, I wouldn't be successful at the end.

REALIZATION OF CMOS COMPATIBLE MICROMACHINED CHEMICAL SENSORS

ABSTRACT

The chemical sensors are fabricated using IC manufacturing technologies, providing a smaller size and lower weight, lower power consumption, and lower cost due to the automated and batch production. During the last two decades, largely two-dimensional Integrated Circuit (IC) fabrication technology has been extended into the third dimension by micromachining technologies [1]. Micromachining has been used to produce a growing variety of micromechanical structures, including automotive pressure sensors, airbag deployment accelerometers and many others [2–4]. Given the similarities in IC fabrication and micromachining, microelectronics and micromechanics may be integrated on a single chip, allowing an on-chip monitoring and control of the mechanical/chemical functions. This has led to the term microelectromechanical systems (MEMS) to describe this technology. The use of MEMS technology could provide a number of opportunities for gas sensors: the sensing elements can be miniaturized (reducing power consumption), multiple elements can be integrated into array configurations with each element optimized to sense a different gas, improved selectivity/sensitivity and the integration of sensing and signal processing/control devices on the same substrate. In addition, due to the small mass of micromachined-sensor element, rapid thermal programming can be employed to introduce a level of kinetic selectivity into the operation of the sensor.

In this thesis, realization of Complementary Metal Oxide Semiconductor (CMOS) compatible chemical sensors using micromachining technology will be explained. During this realization 3x2 sensor array is designed to improve the selectivity and sensitivity of the sensor system. To address the needs of convenient and batch processes CMOS compatibility is incorporated inside the fabrication flow because CMOS compatibility offers convenient merging with read-out circuitry which comprises of operational transconductance amplifiers(OTAs). OTAs are preferred in this design because they assist the detection of the resistance changes at the sensor output.

ÖZET

Günümüzde toplum, çevre ve sağlık konusunda daha duyarlıdır. Bunun sonucu olarak, özellikle gelişen sanayi ve teknoloji ile birlikte, çevremizde bulunup, sağlığımızı etkileyen kimyasalların hızlı ve seçici bir şekilde algılanması daha da önem kazanmıştır. Değişik devre formlarında (pasif-resistör, aktif-mikroelektronik, akustik dalga), yarı-iletken tipi sensörler, 1960'lı yılların başından günümüze kadar, ticari uygulamalarda, bio-medikal, savunma ve endüstri alanlarında, kimyasalların türü ve miktarının ölçümünde yaygın olarak kullanılmaktadır. Bu tür devrelerin temel değerlendirme kriterleri; operasyonun basitliği, yapısının küçüklüğü, maliyetinin ucuz olması, uzun ömürlü olması, tepkinin tekrarlanabilmesi, hassasiyeti ve seçiciliğidir.

Pozlama, ince film, aşındırma, difüzyon ve yarı-iletken teknolojisinde meydana gelen gelişmeler, bugün kullandığımız yüksek hızda, düşük boyut ve fiyatlı entegre devrelerin üretimine imkan sağlamıştır. Daha çok iki boyutlu olan bu üretim teknolojisine, özel aşındırıcılar, aşındırma durdurma teknikleri ve geçici katmanların kombinasyonundan oluşan mikroişleme teknolojisi de eklenerek, üçüncü bir boyut kazandırılmıştır. Mikroişleme, mikron boyutlu yapıların üretimi için kullanılan tekniklerin genel adıdır. Mikroişleme tekniklerinin en önemli ayrıcalığı tümdevre (IC) yapımında kullanılan mikroelektronik endüstrisiyle aynı teknolojiyi kullanmasıdır. Bu iki üretim teknolojilerinin biriri ile olan benzerliği kullanılarak, mekanik yapıların ve bunları kontrol eden ve gözetleyen elektronik devrelerin aynı taban üzerinde gerçekleşmeleri sağlanarak, mikroeletromekanik (MEMS) yapıları oluşturulmuştur.

Bu tezde, MEMS teknolojisi kullanılarak, performans parametreleri iyileştirilmiş kimyasal sensörlerinin ve sensör seçimine karar veren ve sinyali algılanabilir şekilde işleyen okuma ve kontrol tüm devrelerinin tasarımı ve üretimi gerçekleştirilmiştir. Bu amaçla matrisel yapılar kullanarak, seçiciliği ve duyarlılığı yüksek sensör sistemi ve yüksek sıcaklıkta ve düşük güç sarfiyatında çalışacak şekilde tasarlanmış ve simulasyon ile görülmüştür. Sensör sinyali işlenmesi için yüksek kazanç ve geniş bantlı işlemsel kuvvetlendirici tasarlanmış ve üretilmiştir.

TABLE OF CONTENTS

ACKNOWLEDGMENTS	v
ABSTRACT	vi
ÖZET	vii
1 INTRODUCTION	1
2 CHEMICAL SENSORS: THEORY & DESIGN	3
2.1 Sensors Used For Detection of Combustible Gases	3
2.1.1 Acoustic Chemical Sensors	4
2.1.1.1 Bulk Acoustic Wave (BAW) Devices	4
2.1.1.2 Surface Acoustic Wave (SAW) Devices	5
2.1.2 Optical Sensors	6
2.1.3 MOSFET Chemical Sensor	7
2.1.4 Metal-Oxide Semiconductor Chemical Sensor	8
2.2 Micromachining Technology	10
2.2.1 Bulk Micromachining	10
2.2.2 Surface Micromachining	11
2.3 Fabrication Steps of Designed Chemical Sensor	12
2.3.1 Chemical Sensor Requirements	13
2.3.2 Sensor Arrays	15
3 ELECTRO-THERMAL AND MECHANICAL SIMULATIONS	17
3.1 Heat Transfer	17
3.1.1 Conduction	18
3.1.2 Convection	20
3.1.3 Radiation	20
3.2 Electro-thermal Behavior of Micromachined Chemical Sensors	21
3.3 Mechanical Modelling of Micromachined Chemical Sensors	23
3.4 Simulation Results	24
4 DESIGN OF ELECTRONIC CIRCUITRY OF CHEMICAL SENSORS	27
4.1 Interface Circuits Used In Chemical Sensors	27
4.1.1 Resistive Type Sensors	27
4.1.1.1 Voltage Dividers	28

4.1.1.2	The Wheatstone Bridge	29
4.1.2	Operational Amplifiers	30
4.2	Design of Operational Transconductance Amplifiers (OTAs)	32
4.3	Design of Current Mirrors	35
4.3.1	DC Performance of Current Mirrors	36
4.3.2	AC Performance of Current Mirrors	38
4.3.3	Application to Conventional Symmetrical OTA	40
4.3.4	Current Mirror Design Used in the Tail of OTA	41
4.4	Simulation Results of the Designed OTA	42
4.5	Integration of the Operational Amplifier and Chemical Sensor	44
5	CONCLUSIONS AND FUTURE WORK	50
	APPENDIX	52
A	MAXIMUM ALLOWABLE CONCENTRATIONS OF COMBUSTIBLE GASES	52
B	DETAILED FABRICATION STEPS OF CHEMICAL SENSOR	54
C	MASK LAYOUTs OF CHEMICAL SENSORS AND ITS INTERFACE CIRCUITRY	60
	BIBLIOGRAPHY	61

LIST OF FIGURES

2.1	Basic structures of n-channel (a)MISFET and (b)MISCAP which operate on the same basic principle but differ in measurands	7
2.2	Frontside bulk etching	11
2.3	Backside bulk etching	12
2.4	Surface micromachining: (a) patterned sacrificial layer; (b) patterned structural layer (c) suspended beam after sacrificial etching	13
2.5	Sensor structure	14
2.6	Fabrication steps of designed TiO ₂ based chemical sensor	15
2.7	Schematic representation of sensor array	16
3.1	Heat fluxes of a micromachined chemical sensor	21
3.2	(a) Temperature distribution on the stacked membrane. 500°C was obtained with power consumption less than 100 mW. (b) Stress distribution on the stacked membrane in the Z direction.	26
4.1	Voltage divider	28
4.2	Wheatstone bridge	30
4.3	Simplified model of operational amplifiers	31
4.4	Operational amplifier having negative feedback loop	31
4.5	Symbol of differential input OTA	32
4.6	Simple differential input OTA	32
4.7	An OTA with an improved output swing	33
4.8	The signal paths of the OTA in Fig. 4.7	33
4.9	An OTA with improved output impedance	35
4.10	An OTA with improved load current using 1:B current mirrors.	36

4.11	The schematic representation of OTA which is designed using AMS 0.6 μm technology	37
4.12	N-channel current mirror	37
4.13	Small signal model of current mirror shown in simple N-channel current mirror	39
4.14	The small-signal equivalent circuit of the output of the basic current mirror .	40
4.15	I_2 vs V_{DS2} curves	41
4.16	Cascode current mirror (used in the designed OTA)	42
4.17	Small-signal model of the current mirror of Fig. 4.16.	42
4.18	I_2 vs V_{DS2} curves for cascoded current mirror	43
4.19	Open-loop AC characteristic of OTA: Gain at low frequencies: 41.7 dB, bandwidth: 23 MHz., Gain \times Bandwidth: 700 MHz.	43
4.20	Negative feedback inverting type closed-loop AC characteristic of OTA: 700 MHz.	45
4.21	Transient response of OTA when 1 MHz sinusoidal source is applied to the differential input	46
4.22	Transient response of OTA when 10 MHz sinusoidal source is applied to the differential input	46
4.23	Transient response of OTA when 5 MHz pulse is applied to the differential input	47
4.24	Transient response of OTA when 10 MHz pulse is applied to the differential input	47
4.25	Transient response of OTA when 20 MHz pulse is applied to the differential input	48
4.26	Two-stage negative feedback op-amp circuitry for gas sensing	48
4.27	Ideal response of Fig. 4.26	48
4.28	Simulation results of Fig. 4.26	49
C.1	Mask layout of 3x2 sensor system and 2x1 test sensor	60
C.2	Mask layout of operational transconductance amplifier	61

LIST OF TABLES

2.1	Bulk vs. Surface Micromachining	11
3.1	Stacked layer thickness vs. intrinsic pressure	24
3.2	Material Properties	25
3.3	Simulation Results	25
4.1	Dimensions of the elements used in the design of OTA	44
A.1	Threshold Limit Values (Maximum allowable concentrations)	52

**REALIZATION OF CMOS COMPATIBLE MICROMACHINED CHEMICAL
SENSORS**

by
TUĞBA DEMİRCİ

Submitted to the Graduate School of Engineering and Natural Sciences
in partial fulfillment of
the requirements for the degree of
Master of Science

Sabancı University

Spring 2002

REALIZATION OF CMOS COMPATIBLE MICROMACHINED CHEMICAL SENSORS

APPROVED BY

Assist. Prof. Dr. Yaşar GÜRBÜZ
(Thesis Supervisor)

Assist. Prof. Dr. Ayhan BOZKURT

Assist. Prof. Dr. Mehmet KESKİNÖZ

DATE OF APPROVAL:

©Tuğba Demirci 2002

All Rights Reserved

to my parents

&

my brothers

ACKNOWLEDGMENTS

There are some people, without whom this thesis would not have come to existence.

First, I would like to express my endless appreciation to my advisor Yaşar Gürbüz. I am grateful for his patient guidance, support and encouragement in all aspects of this work. I would like to thank Ayhan Bozkurt for his help especially with the learning and using ANSYS for the simulations of the design.

Then, I would like to thank Prof. Yusuf Leblebici for his valuable guidance and support.

Furthermore, I would like to thank Ayça Çesmelioglu, Beril Çiftçi, Emrah Üstünay, Gamze Yurttutan, Özhan Öztürk, Mansoor Naseer, Mustafa Parlak, Müge Şahin and Sanem Kabadayı for their friendship and making my life at SabancıUniversity colorful. I also wish to thank our master Bülent Köroğlu (Bülent Abi) for his precious help.

Lastly, I would like to thank my parents for everything they give me and provide especially during my 18-year-school life. Without them, I wouldn't be successful at the end.

REALIZATION OF CMOS COMPATIBLE MICROMACHINED CHEMICAL SENSORS

ABSTRACT

The chemical sensors are fabricated using IC manufacturing technologies, providing a smaller size and lower weight, lower power consumption, and lower cost due to the automated and batch production. During the last two decades, largely two-dimensional Integrated Circuit (IC) fabrication technology has been extended into the third dimension by micromachining technologies [1]. Micromachining has been used to produce a growing variety of micromechanical structures, including automotive pressure sensors, airbag deployment accelerometers and many others [2–4]. Given the similarities in IC fabrication and micromachining, microelectronics and micromechanics may be integrated on a single chip, allowing an on-chip monitoring and control of the mechanical/chemical functions. This has led to the term microelectromechanical systems (MEMS) to describe this technology. The use of MEMS technology could provide a number of opportunities for gas sensors: the sensing elements can be miniaturized (reducing power consumption), multiple elements can be integrated into array configurations with each element optimized to sense a different gas, improved selectivity/sensitivity and the integration of sensing and signal processing/control devices on the same substrate. In addition, due to the small mass of micromachined-sensor element, rapid thermal programming can be employed to introduce a level of kinetic selectivity into the operation of the sensor.

In this thesis, realization of Complementary Metal Oxide Semiconductor (CMOS) compatible chemical sensors using micromachining technology will be explained. During this realization 3x2 sensor array is designed to improve the selectivity and sensitivity of the sensor system. To address the needs of convenient and batch processes CMOS compatibility is incorporated inside the fabrication flow because CMOS compatibility offers convenient merging with read-out circuitry which comprises of operational transconductance amplifiers (OTAs). OTAs are preferred in this design because they assist the detection of the resistance changes at the sensor output.

ÖZET

Günümüzde toplum, çevre ve sağlık konusunda daha duyarlıdır. Bunun sonucu olarak, özellikle gelişen sanayi ve teknoloji ile birlikte, çevremizde bulunup, sağlığımızı etkileyen kimyasalların hızlı ve seçici bir şekilde algılanması daha da önem kazanmıştır. Değişik devre formlarında (pasif-resistör, aktif-mikroelektronik, akustik dalga), yarı-iletken tipi sensörler, 1960'lı yılların başından günümüze kadar, ticari uygulamalarda, bio-medikal, savunma ve endüstri alanlarında, kimyasalların türü ve miktarının ölçümünde yaygın olarak kullanılmaktadır. Bu tür devrelerin temel değerlendirme kriterleri; operasyonun basitliği, yapısının küçüklüğü, maliyetinin ucuz olması, uzun ömürlü olması, tepkinin tekrarlanabilmesi, hassasiyeti ve seçiciliğidir.

Pozlama, ince film, aşındırma, difüzyon ve yarı-iletken teknolojisinde meydana gelen gelişmeler, bugün kullandığımız yüksek hızda, düşük boyut ve fiyatlı entegre devrelerin üretimine imkan sağlamıştır. Daha çok iki boyutlu olan bu üretim teknolojisine, özel aşındırıcılar, aşındırma durdurma teknikleri ve geçici katmanların kombinasyonundan oluşan mikroişleme teknolojisi de eklenerek, üçüncü bir boyut kazandırılmıştır. Mikroişleme, mikron boyutlu yapıların üretimi için kullanılan tekniklerin genel adıdır. Mikroişleme tekniklerinin en önemli ayrıcalığı tümdevre (IC) yapımında kullanılan mikroelektronik endüstrisiyle aynı teknolojiyi kullanmasıdır. Bu iki üretim teknolojilerinin biriri ile olan benzerliği kullanılarak, mekanik yapıların ve bunları kontrol eden ve gözetleyen elektronik devrelerin aynı taban üzerinde gerçekleştirilmesi sağlanarak, mikroeletromekanik (MEMS) yapıları oluşturulmuştur.

Bu tezde, MEMS teknolojisi kullanılarak, performans parametreleri iyileştirilmiş kimyasal sensörlerinin ve sensör seçimine karar veren ve sinyali algılanabilir şekilde işleyen okuma ve kontrol tüm devrelerinin tasarımı ve üretimi gerçekleştirilmiştir. Bu amaçla matrisel yapılar kullanarak, seçiciliği ve duyarlılığı yüksek sensör sistemi ve yüksek sıcaklıkta ve düşük güç sarfiyatında çalışacak şekilde tasarlanmış ve simulasyon ile görülmüştür. Sensör sinyali işlenmesi için yüksek kazanç ve geniş bantlı işlemsel kuvvetlendirici tasarlanmış ve üretilmiştir.

TABLE OF CONTENTS

ACKNOWLEDGMENTS	v
ABSTRACT	vi
ÖZET	vii
1 INTRODUCTION	1
2 CHEMICAL SENSORS: THEORY & DESIGN	3
2.1 Sensors Used For Detection of Combustible Gases	3
2.1.1 Acoustic Chemical Sensors	4
2.1.1.1 Bulk Acoustic Wave (BAW) Devices	4
2.1.1.2 Surface Acoustic Wave (SAW) Devices	5
2.1.2 Optical Sensors	6
2.1.3 MOSFET Chemical Sensor	7
2.1.4 Metal-Oxide Semiconductor Chemical Sensor	8
2.2 Micromachining Technology	10
2.2.1 Bulk Micromachining	10
2.2.2 Surface Micromachining	11
2.3 Fabrication Steps of Designed Chemical Sensor	12
2.3.1 Chemical Sensor Requirements	13
2.3.2 Sensor Arrays	15
3 ELECTRO-THERMAL AND MECHANICAL SIMULATIONS	17
3.1 Heat Transfer	17
3.1.1 Conduction	18
3.1.2 Convection	20
3.1.3 Radiation	20
3.2 Electro-thermal Behavior of Micromachined Chemical Sensors	21
3.3 Mechanical Modelling of Micromachined Chemical Sensors	23
3.4 Simulation Results	24
4 DESIGN OF ELECTRONIC CIRCUITRY OF CHEMICAL SENSORS	27
4.1 Interface Circuits Used In Chemical Sensors	27
4.1.1 Resistive Type Sensors	27
4.1.1.1 Voltage Dividers	28

4.1.1.2	The Wheatstone Bridge	29
4.1.2	Operational Amplifiers	30
4.2	Design of Operational Transconductance Amplifiers (OTAs)	32
4.3	Design of Current Mirrors	35
4.3.1	DC Performance of Current Mirrors	36
4.3.2	AC Performance of Current Mirrors	38
4.3.3	Application to Conventional Symmetrical OTA	40
4.3.4	Current Mirror Design Used in the Tail of OTA	41
4.4	Simulation Results of the Designed OTA	42
4.5	Integration of the Operational Amplifier and Chemical Sensor	44
5	CONCLUSIONS AND FUTURE WORK	50
	APPENDIX	52
A	MAXIMUM ALLOWABLE CONCENTRATIONS OF COMBUSTIBLE GASES	52
B	DETAILED FABRICATION STEPS OF CHEMICAL SENSOR	54
C	MASK LAYOUTs OF CHEMICAL SENSORS AND ITS INTERFACE CIRCUITRY	60
	BIBLIOGRAPHY	61

LIST OF FIGURES

2.1	Basic structures of n-channel (a)MISFET and (b)MISCAP which operate on the same basic principle but differ in measurands	7
2.2	Frontside bulk etching	11
2.3	Backside bulk etching	12
2.4	Surface micromachining: (a) patterned sacrificial layer; (b) patterned structural layer (c) suspended beam after sacrificial etching	13
2.5	Sensor structure	14
2.6	Fabrication steps of designed TiO ₂ based chemical sensor	15
2.7	Schematic representation of sensor array	16
3.1	Heat fluxes of a micromachined chemical sensor	21
3.2	(a) Temperature distribution on the stacked membrane. 500°C was obtained with power consumption less than 100 mW. (b) Stress distribution on the stacked membrane in the Z direction.	26
4.1	Voltage divider	28
4.2	Wheatstone bridge	30
4.3	Simplified model of operational amplifiers	31
4.4	Operational amplifier having negative feedback loop	31
4.5	Symbol of differential input OTA	32
4.6	Simple differential input OTA	32
4.7	An OTA with an improved output swing	33
4.8	The signal paths of the OTA in Fig. 4.7	33
4.9	An OTA with improved output impedance	35
4.10	An OTA with improved load current using 1:B current mirrors.	36

4.11	The schematic representation of OTA which is designed using AMS 0.6 μm technology	37
4.12	N-channel current mirror	37
4.13	Small signal model of current mirror shown in simple N-channel current mirror	39
4.14	The small-signal equivalent circuit of the output of the basic current mirror .	40
4.15	I_2 vs V_{DS2} curves	41
4.16	Cascode current mirror (used in the designed OTA)	42
4.17	Small-signal model of the current mirror of Fig. 4.16.	42
4.18	I_2 vs V_{DS2} curves for cascoded current mirror	43
4.19	Open-loop AC characteristic of OTA: Gain at low frequencies: 41.7 dB, bandwidth: 23 MHz., Gain \times Bandwidth: 700 MHz.	43
4.20	Negative feedback inverting type closed-loop AC characteristic of OTA: 700 MHz.	45
4.21	Transient response of OTA when 1 MHz sinusoidal source is applied to the differential input	46
4.22	Transient response of OTA when 10 MHz sinusoidal source is applied to the differential input	46
4.23	Transient response of OTA when 5 MHz pulse is applied to the differential input	47
4.24	Transient response of OTA when 10 MHz pulse is applied to the differential input	47
4.25	Transient response of OTA when 20 MHz pulse is applied to the differential input	48
4.26	Two-stage negative feedback op-amp circuitry for gas sensing	48
4.27	Ideal response of Fig. 4.26	48
4.28	Simulation results of Fig. 4.26	49
C.1	Mask layout of 3x2 sensor system and 2x1 test sensor	60
C.2	Mask layout of operational transconductance amplifier	61

LIST OF TABLES

2.1	Bulk vs. Surface Micromachining	11
3.1	Stacked layer thickness vs. intrinsic pressure	24
3.2	Material Properties	25
3.3	Simulation Results	25
4.1	Dimensions of the elements used in the design of OTA	44
A.1	Threshold Limit Values (Maximum allowable concentrations)	52

CHAPTER 1

INTRODUCTION

Due to society's concern with the environment and the industry's need of operating under ever more demanding conditions, the need for gas sensors to detect, monitor, and control various chemical species with a better sensitivity, selectivity, reproducibility and rapid response at reasonable cost becomes more obvious. Among others, semiconductor type gas sensors have been used for 30 years [7]. They rely on the interactions between certain ambient species and the active portion of the sensing device. The magnitude of the change is mostly related to the concentration and kind of gas components, structural properties of the sensing device and operating temperature. High temperature operation/compatibility of these sensors are highly desirable in many applications (such as automotive, environment, process control etc.) due to the improved sensing performance in most cases (i.e., faster/higher response rate, higher sensitivity and selectivity) [8–10].

Since CMOS (Complementary Metal Oxide Semiconductor) technology has become the dominant technology in IC (Integrated Circuit) design, a variety of microsensors have begun to use this technology to provide on-chip fabrication of both the sensors and their electronic circuitry. As a result, micromachining technology has developed rapidly over fifteen years ago using the materials processed in the integrated circuit technology to form miniature structures other than electronic circuits. Therefore, the fabrication of solid-state sensors has been the main trust of micromachining technology. The term MEMS (MicroElectroMechanical Systems) is an expansion of this technology. Improvements possible with MEMS technology involve the expanded range of materials and processes that can be employed, the precise dimensional scale and mechanical complexity that can be achieved in devices, and expanded capabilities for electronic integration. In this thesis work, it is aimed to achieve to design and fabricate solid-state gas sensor and its read-out and control circuitry using

MEMS technology.

A semiconductor chemical sensor is a device that translates a change in a chemical quantity of a gas ambient into a measurable electrical quantity. A gas sensor is, therefore, a “bridge” between the physical world and the electronic system. A lot of research and development is done to design small and cheap chemical sensors which possess high sensitivity, selectivity and stability. This search comes along with a large variety of sensors based on different sensing principles such as semiconductor gas sensors, optical sensors, thermal conductivity sensors and mass sensitive devices like quartz microbalance sensors.

The idea of using semiconductors as gas sensitive devices leads back to 1952 when Brattain and Bardeen first reported gas sensitive effects of Germanium [11]. Later, Seiyama found gas sensing effect on metal oxides [12]. Taguchi finally brought semiconductor sensors based on metal oxides to an industrial product [5–7]. The first hydrogen sensitive metal oxide semiconductor (MOS) field effect transistor were published in 1975 by Lundstrom. This device was a Pd-gate MOS transistor with very thin oxide and Pd layers (about 10 nm). The gas sensitivity was observed in transistors and capacitors with both thin and thick oxide and Pd layers. Molecular hydrogen dissociates to atomic hydrogen on the palladium surface. The atomic hydrogen diffuses into the palladium film and some of it adsorbs at the inner palladium surface. The adsorbed hydrogen atoms act as dipoles at the metal-insulator interface and give rise to a change in the work function of the metal at the interface, which affects the threshold voltage of a transistor.

The focus of this thesis is on semiconductor type chemical sensors based on metal oxides. Their advantages are good selectivity to some relevant gases like CO, H₂, NO_x and hydrocarbons, simple data processing, low production cost and small size [13]. The operational principle of this type of sensors rely on the interactions between certain ambient species and active portion (metal oxide) of the sensing device. The magnitude of the change is mostly related to the concentration and type of gas components, structural properties of the sensing device and operating temperature.

This thesis is organized as follows. Chapter 2 discusses brief information about the commercially available chemical sensors and their operational principles. Furthermore, in this chapter, the details of micromachining, its compatibility with IC technology and its use in chemical sensor design are explained. The structural and thermal simulations of chemical sensors are given in Chapter 3. In Chapter 4, the signal processing circuits of chemical sensor are introduced and the simulation results of the designed circuitry are given. Finally in Chapter 5, the conclusion and future work are presented.

CHAPTER 2

CHEMICAL SENSORS: THEORY & DESIGN

There is currently a need for low cost portable instrumentation to detect the chemicals with high selectivity and sensitivity. To meet this need, there have been many valuable researches made for almost 30 years [29, 30]. These type of instruments should include the control systems, comprised of IC electronic circuitry, together with them in order to manage the online monitoring of the gases in the environment. Therefore, the IC compatibility becomes more important for that kind of system. In this chapter, different types of commercially available chemical sensors which are sensitive to combustible gases are examined, their fabrication techniques and details of the designed sensor are presented. Micromachining technology was used to fabricate our sensor system because of its IC compatibility and its suitability for producing the sensors in an array configuration in order to obtain high selectivity.

2.1 Sensors Used For Detection of Combustible Gases

The sensing principle used in silicon chemical sensors for combustible gas detection are mainly electrochemical, optical and acoustical. Acoustic-wave sensors, optical sensors using integrated optics or optical fibers, metal oxide semiconductor and MOSFET sensors fabricated on silicon substrates are commonly used chemical sensors. The first two are mass-based chemical sensors while the later two are electric-based chemical sensors [14–16].

2.1.1 Acoustic Chemical Sensors

There are two type of acoustic chemical sensors namely bulk and surface acoustic wave devices. Both of them employ piezoelectric crystals that are deformed mechanically by applying a potential or voltage in order to generate acoustic waves that can travel either through the bulk of the crystal or along its surface. These devices are useful for chemical sensing because both the velocity and the frequency of the waves depends on the mass of the crystal [17].

2.1.1.1 Bulk Acoustic Wave (BAW) Devices

The concept of bulk acoustic devices started with the quartz crystal microbalance (QCM) and first applied to organic vapour sensing. QCM utilizing bulk acoustic wave in piezoelectric materials is probably the simplest type of gas sensor using piezoelectric device [14]. Rock crystal such as single crystal quartz has an interesting property in which it is distorted by applied electric voltage while an electric field is generated by applied pressure. This phenomenon is called the piezoelectric effect. Because of this effect, upon excitation by application of a suitable ac voltage across the quartz crystal, the crystal can be made to oscillate at a characteristic resonant frequency. QCM gas sensor comprises a slice of single crystal of quartz, typically around 1 cm in diameter, with thin-film gold electrodes which are evaporated onto both surfaces of sliced crystal. The quartz crystal oscillates in such manner that particle displacements on the QCM sensor surface are normal to the direction of wave propagation.

The thickness of the quartz crystal, determines the wavelength of the fundamental and harmonics of oscillation. The resonant frequency of the QCM sensor is related to the change of the mass of QCM loading by the Sauerbrey equation [18]

$$\Delta f = -2f_0^2 m_f / A(\rho_q \mu_q)^{1/2} \quad (2.1)$$

where Δf is the change in resonant frequency, f_0 is the resonant frequency, m_f is the mass change due to adsorption of gases, A is the electrode area, ρ_q is the density of quartz and μ_q is the shear modulus. For typical quartz crystal operating at 10 MHz, a mass change of

the order of 1 nano gram produces a frequency change of about 1 Hz. Thus small changes in mass can be measured using QCM coated with molecular recognition membrane on which gas molecules are adsorbed.

The selectivity of the QCM sensor is determined by the coating membrane deposited on the surface of the crystal.

2.1.1.2 Surface Acoustic Wave (SAW) Devices

The idea has been extended to SAW devices and later to other configurations using different types of guided acoustic waves. If the acoustic sensor is coated with a chemically selective layer and if appropriate signal processing is used, a chemical sensor can be constructed, and the composition and concentration of gas mixtures can be determined.

The SAW device is made of relatively thick plate of piezoelectric materials (ZnO and lithium niobate) with interdigitated electrodes to excite the oscillation of the surface wave. The SAW is stimulated by applying an a.c. voltage to the fingers of an interdigitated electrode to lead to a deformation of piezoelectric crystal surface [19–21]. The SAW devices are usually operated in one of two configurations such as a delay line and a resonator. In both cases, the propagation of SAW is affected by changes in the properties of the piezoelectric crystal surface. In a common gas sensor using SAW device with a dual, delay line structure, one arm of the delay line is coated with the sorbent membrane, the other acts as a reference to reduce the change of environmental conditions such as temperature drift and other effects. The change in frequency of the SAW with sorption of vapour, Δf_v , is given by

$$\Delta f_v = \delta f_p c_v K_p / \rho_p \quad (2.2)$$

for a simple mass loading effect, where Δf_p is the change in frequency caused by membrane itself, c_v is the vapour concentration, K_p is the partition coefficient and ρ_p is the density of the membrane used. The main problems with SAW gas sensor are a relatively poor long term stability and a high sensitivity to humidity.

2.1.2 Optical Sensors

Optical techniques for chemical analysis are well established. Sensors based on these techniques are now attracting considerable attention because of their importance in applications such as environmental monitoring, biomedical sensing, and industrial process control. In many instances these sensors exploit specific advantages of optical fiber technology. Fiber-optic chemical sensors (FOCS) can benefit from, for example, the geometric versatility, low attenuation, and electrical noise immunity of optical fibers [17].

In recent years, an increased research effort has been focused on the investigation of approaches for the application of porous layers coated on fibre substrates and prepared to fiber-optic chemical sensing. For this purpose, changes of optical properties of porous layers, such as refractive index, optical absorption or fluorescence, induced by the penetration of detected substances into these layers - the detection site - are measured by means of substrate optical fibers. In this way, porous silica layers coated on silica fibers have been employed for the detection of vapours of organic solvents changing the refractive index of layers.

The determination of changes of optical properties of porous layers in fiber-optic chemical sensors is based on the fact that these changes modify the amplitudes and (/or) phases of optical waves propagating in the fibre which effects can be determined by measurements at the end of the fibre. Therefore, both the properties of these layers and their changes induced by the detected chemicals are important for the sensitivity of fiber-optic chemical sensors.

Surface Plasmon Resonance (SPR) is an optical phenomenon in which incident light excites a charge-density wave at the interface between a highly conductive metal and a dielectric material. The conditions for excitation are determined by the permittivities of the metal and the dielectric material. The SPR transduction principle is widely used as an analytic tool for measuring small changes in the refractive index of a thin region adjacent to the metal surface. The optical excitation of surface plasmon on a thin metallic film has been recognized as a promising technique for sensitive detection of chemical species such as odor, vapour or liquid [22]. Several methods have been employed to monitor the excitation of SPR by measuring the light reflected from the sensor interface. These include analysis of angle modulation [23], wavelength modulation [24], intensity modulation [25] and phase modulation [26].

Optical SPR sensors are sensitive to change in the refractive index of a sample surface. Recently, it has been reported that toxic gases such as ammonia, toluene, xylene, ethylac-

etate, 4-methyl-2-pentanone and propionic acid can be detected by measuring the SPR using angle modulation [27].

2.1.3 MOSFET Chemical Sensor

The gas sensors utilizing the electrical characteristics of Schottky diodes and MOSFET are based on the work function change of some catalytic metals such as palladium and platinum by the presence of chemical species at their surfaces. The gas sensors using MOSFET is based on metal-insulator-semiconductor structures in which the metal gate is a catalyst for gas sensing.

The micro chemical sensor using structure of a MOSFET in which the gate is made of a gas sensitive metal such as Pd first proposed by Lundstrom in 1975 [29]. This sensor exhibited a threshold voltage shift depending upon the gas concentration and was particularly sensitive to hydrogen down to the ppm level with maximum threshold voltage shift about 0.5 V. The use of other metal gate materials such as Pt and Ir and operating the sensors at different temperatures has led to reasonable selectivity to gases such as NH_3 , H_2S and ethanol [30].

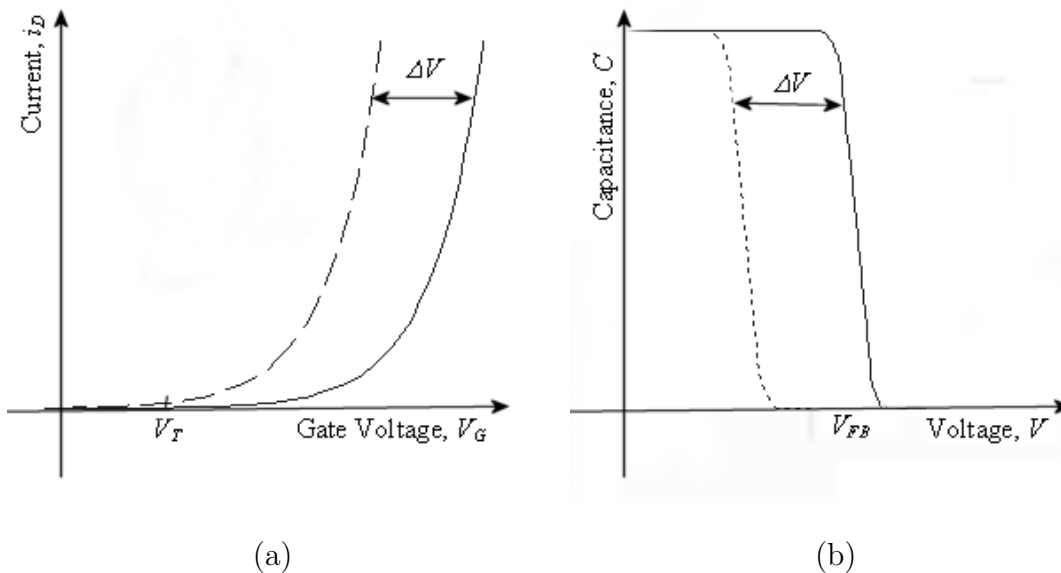


Figure 2.1: Basic structures of n-channel (a) MISFET and (b) MISCAP which operate on the same basic principle but differ in measurands

There are two basic structures such as MISFIT (Metal-Insulator-Semiconductor Field Effect Transistor) and MISCAP (Metal-Insulator-Semiconductor CAPacitor). The basic

structures of n-channel MISFET and MISCAP which operate on the same basic principle but differ in measurands are shown in Fig. 2.1. In the MISFET the drain current i_D flowing through the semiconductor is controlled by the surface potential due to applied gate voltage V_G , and in the MISCAP the capacitance of the MIS structure is determined by the surface potential. These devices can respond to exposure to any gas which changes the surface potential or the work function of the gate metal.

2.1.4 Metal-Oxide Semiconductor Chemical Sensor

The metal oxides such as SnO_2 , ZnO , TiO_2 , Fe_2O_3 and WO_3 are n type semiconductors. At the temperatures of 200-500°C, these n-type metal oxide semiconductors respond to reducing gases such as H_2 , CH_4 , CO , C_2H_5 or H_2S and increase their conductivity [28]. The conductivity σ or the resistivity ρ of these metal oxide semiconductors is given by

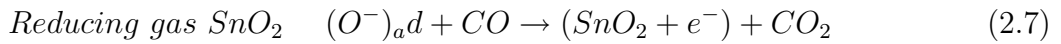
$$\sigma = 1/\rho = en\mu \quad (2.3)$$

where e is the charge of electron (1.6022×10^{-19} C), n the carrier (electron) concentration (cm^{-3}) and μ is the carrier mobility (cm^2/Vs). In the atmospheric air some oxygen atoms is adsorbed on the surface of n-type semiconductor to trap a free electron from semiconductor metal oxide and consequently high resistive layer is produced in the vicinity of the semiconductor surface. Furthermore, the electrically double layer which acts as the scattering center for conducting electrons is created by means of adsorption of oxygen atoms on the semiconductor surface and at grain boundaries of polycrystalline semiconductors. Therefore, if the adsorbed oxygen atoms are consumed by the oxidizing reaction on the surface and at the grain boundaries and consequently free electrons are increased and the scattering centers are decreased in the semiconductors to produce the increase in carrier concentration n and mobility μ . This is the mechanism for conductivity increase in the n-type semiconductors when the reducible gases are exposed to the surface of n-type polycrystalline semiconductors. The mechanism of the increase in carrier concentration is



where e is an electron from the conduction band of the oxide semiconductors, $\text{R}(g)$ is the reducible gases, s and g stands for surface and gas, respectively. Eq. 2.4 implies that oxygen

is physico-chemically adsorbed onto lattice vacancies in the oxide semiconductor and consequently the conductivity of the oxide semiconductor becomes lower than that in the case of no adsorbed oxygen. An electron is generated by the reaction with reducible gases R(g) through Eq. 2.5. Consequently, the conductivity is increased following Eq. 2.5 as a result in the increase of carrier concentration. In contrast, p-type semiconductors such as CuO, NiO and CoO respond to oxidizable gases such as O₂, NO₂ and Cl₂.



When the SnO₂ is used as a metal oxide Eq.2.4 and Eq.2.5 become Eq.2.6 and Eq.2.7, respectively. In clean air, oxygen atoms which traps free electrons in the bulk SnO₂, is adsorbed onto the SnO₂ particle surface, forming a potential barrier in the grain boundaries. This potential barrier restricts the flow of electrons, causing the electrical conductivity to decrease, because the potential barrier acts as the scattering center for the electron conduction. When the sensor is exposed to an atmosphere containing reducible gases, e.g. combustible gases, CO and other similar gases, the SnO₂ surface adsorbs these gas molecules and causes oxidation. This lowers the potential barrier, allowing electrons to flow more easily, thereby increasing the electrical conductivity.

The reaction between gases and surface oxygen will vary depending on the operating temperature of sensor and the activity of sensor materials. The increasing sensitivity and selectivity of the sensors for exposure to gases can be realized by incorporation of a small amount of impurities and catalytic metal additives such as palladium (Pd) or platinum (Pt). The impurities act as extrinsic donors (or acceptors) and consequently the conductivity of the sensors can be changed by controlling the amount of impurities doped. Doping of the catalytic metal to sensor or coating with thin catalytic metal film of the sensor surface makes to change in the selectivity of the sensor. As described above, the crystallographical structure of the semiconductors as the sensor material is commonly the polycrystalline. Thus, semiconductors as the sensor material include many grain boundaries. As explain above, the grain boundaries act as the scattering centers for conducting electrons to produce the change of carrier mobility and consequently the crystallinity affects the sensitivity of the sensors.

The most widely used semiconducting material as the gas sensor is SnO₂, doped with small amounts of impurities and catalytic metal additives. By changing the choice of impurity and catalyst and operating condition such as operating temperature, many kind of gas sensors using SnO₂ have been developed for detecting many kinds of gases.

Since our design is based on metal oxide semiconductor type chemical sensor, the detailed information is given in Section 2.2.

2.2 Micromachining Technology

Due to advances in the IC manufacturing technology, the significant progress made in the microsensors and microactuators in recent years. High performance electronic systems using the IC process can be extended to engineering systems that require other than electronic devices. These other devices (usually mechanical) can be produced using steps like those developed for the planar process. Therefore the importance of micromachining technology considering the IC manufacturing technology as a reference has increased. Generally, micromachining technology provides to fabricate mechanical structures with micron sizes. It can be classified into two groups as either bulk micromachining or surface micromachining. In the bulk micromachining technology, the mechanical parts is done by anisotropically etching or machining the bulk substrate while in the surface micromachining technology deposited films are used to make the mechanical parts extending above the surface of the silicon substrate.

Both bulk micromachining and surface micromachining technology provides to extend two dimensional IC fabrication technology into three dimensional technology by using special etchants, etch stops and sacrificial layers. Given the similarities in IC fabrication and micromachining, microelectronics and micromechanics may be integrated on a single chip allowing on-chip monitoring and control of the mechanical structures. Table 2.1 compares the bulk micromachining with the surface micromachining technology.

2.2.1 Bulk Micromachining

Two basic methods are used in order to structure silicon: wet chemical etching and dry etching. The wet chemical etching is performed by anisotropic etchants such as KOH and TMAH. Both chemicals show different etch rates depending on the crystal structure, whereas the etch rate in $\langle 100 \rangle$ direction is much faster than $\langle 111 \rangle$ direction. Fig. 2.2 shows the pyramidal pits etch into (100) oriented silicon using anisotropic wet etchant, bounded by

(111) crystal plane. As shown in Fig. 2.2, the angle between the (111) plane and (100) plane is approximately 54.74° . In Fig. 2.3, the anisotropic backside etch of silicon is illustrated.

Table 2.1: Bulk vs. Surface Micromachining

Features	Bulk Micromachining	Surface Micromachining
Core Material	Silicon	Polysilicon
Sacrificial Layer	—	PSG, SiO ₂
Size	Large (typical cavity dimensions are several hundred μm)	Small (high precision controlled by thickness of the film; typical dimensions are several μm)
Processing factors	Single or double side processing (front and back side) Selectivity in material etching Etching: anisotropic (depends on crystal orientation) Etch stops Patterning	Single side processing (front side) Selectivity in material etching Etching: Isotropic Residual stress in films (depends on deposition, doping, annealing)

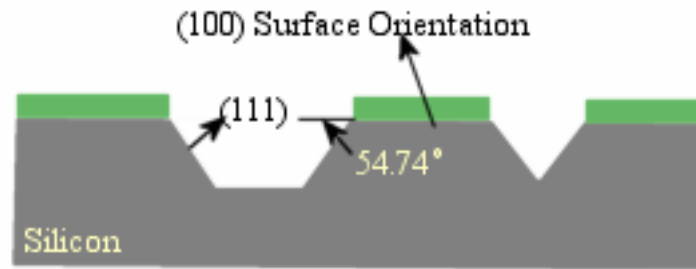


Figure 2.2: Frontside bulk etching

2.2.2 Surface Micromachining

Smaller structures can be processed using surface micromachining technology. Fig. 2.4 depicts the basic concept of surface micromachining. An isolation layer (Si_3N_4) is deposited on a silicon substrate in order to protect the substrate both mechanically and electrically from the top layers deposited above substrate. Then, a sacrificial layer, most commonly

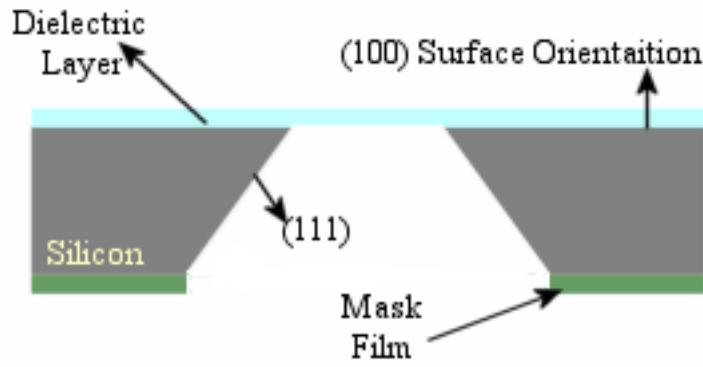


Figure 2.3: Backside bulk etching

SiO_2 , is deposited over the isolation layer and patterned. After sacrificial layer deposition, a structural layer (mainly polysilicon because of its IC compatibility) is deposited. Finally the sacrificial layer is removed to produce the free-standing micromechanical structures.

2.3 Fabrication Steps of Designed Chemical Sensor

The designed sensor shown in Fig. 2.5 is fabricated using bulk micromachining technology. The detailed fabrication steps of the sensor is shown in Fig. 2.6. The more explained fabrication steps are illustrated in Appendix B. There are 2 routing metals seven masks in total and each of the masks layouts is given in Appendix C. The main process steps are

- i) (100) oriented double polished silicon is chosen as a bulk material.
- ii) $\text{SiO}_2/\text{Si}_3\text{N}_4/\text{SiO}_2$ layers are deposited over the substrate.
- iii) Polysilicon layer is then deposited and patterned (Mask 1) to form polysilicon heater.
- iv) Si_3N_4 is deposited and patterned to make heater contacts (Mask2).
- v) Aluminum metal is deposited and patterned (Mask3).
- vi) SiO_2 is deposited.
- vii) Gas sensitive metal oxide (TiO_2) is developed and patterned (Mask 4).
- viii) After patterning gas sensitive layer, the oxide beneath TiO_2 is patterned. This patterning is necessary because the heater should have a contact with the last metal layer (Mask 5) in order to apply voltage.

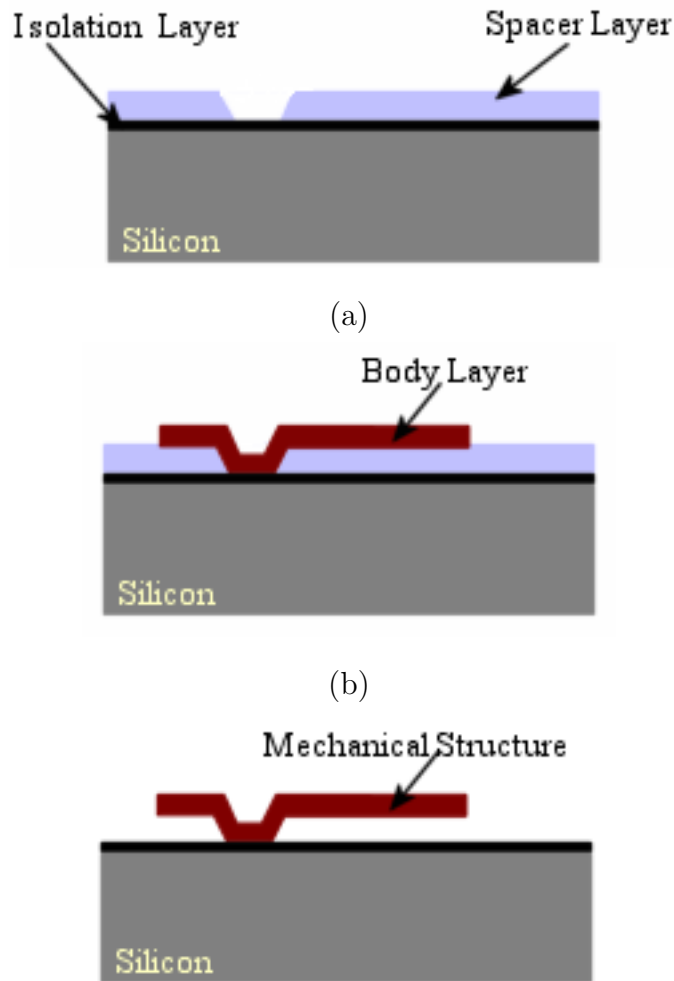


Figure 2.4: Surface micromachining: (a) patterned sacrificial layer; (b) patterned structural layer (c) suspended beam after sacrificial etching

- ix) Second metal is deposited and patterned to make a contact of metal oxide and heater (Mask 6).
- x) Finally after the passivation layer deposition the backside of silicon substrate is removed. (Mask 7).

2.3.1 Chemical Sensor Requirements

The essential properties of chemical sensors can be summarized as follows:

1. Selectivity:

The chemical sensor must respond to a wide range of chemical species to be detected.

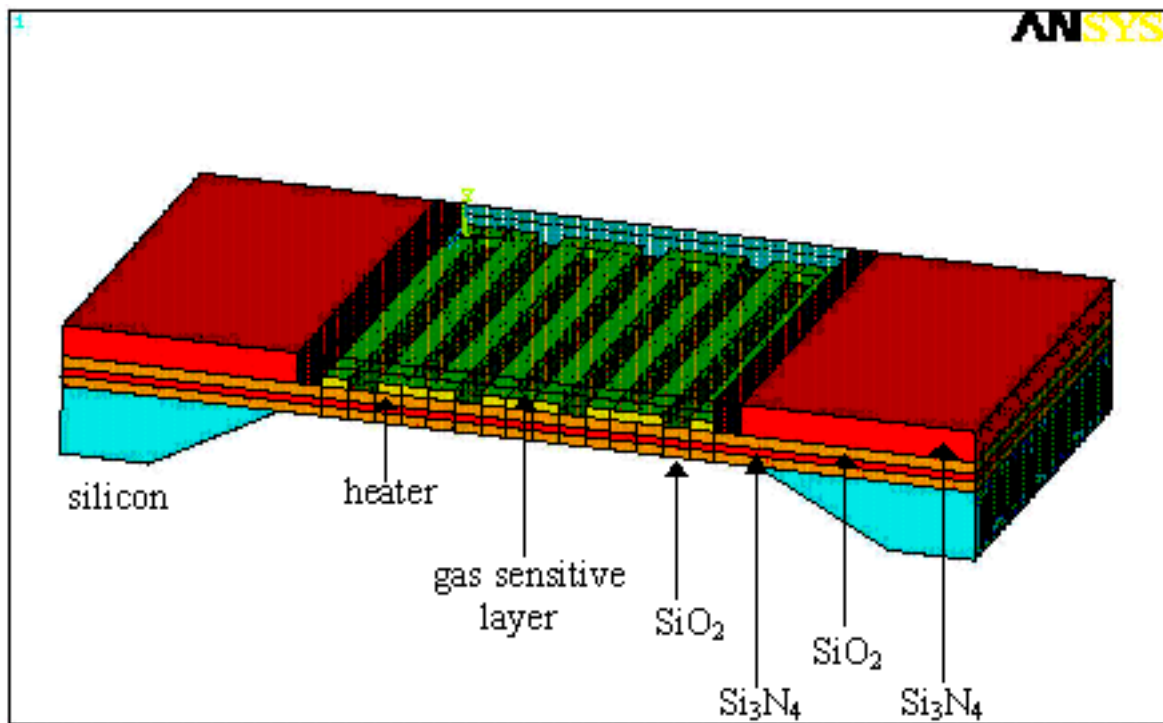


Figure 2.5: Sensor structure

The sensors should not have overlapping sensitivities to discriminate among different chemical species.

2. Sensitivity:

The chemical sensor must be sensitive to small concentration levels.

3. Speed of response:

The response time of the sensor should be in seconds in order to achieve online monitoring.

4. Reproducibility:

The individual sensor element should be reproducible in its manufacture and response characteristic. This will reduce the task of calibrating each sensor element before use. Fabrication processes used to make a single sensor element must be compatible with the manufacture of an array of reasonable size. Furthermore, the sensor should have a linear response characteristic.

5. Reversibility:

The sensors must recover after the exposure of gas. If the process of the absorption of gas in the metal oxide is completely reversible, the sensor will not degrade and the response will not drift in the subsequent cycles.

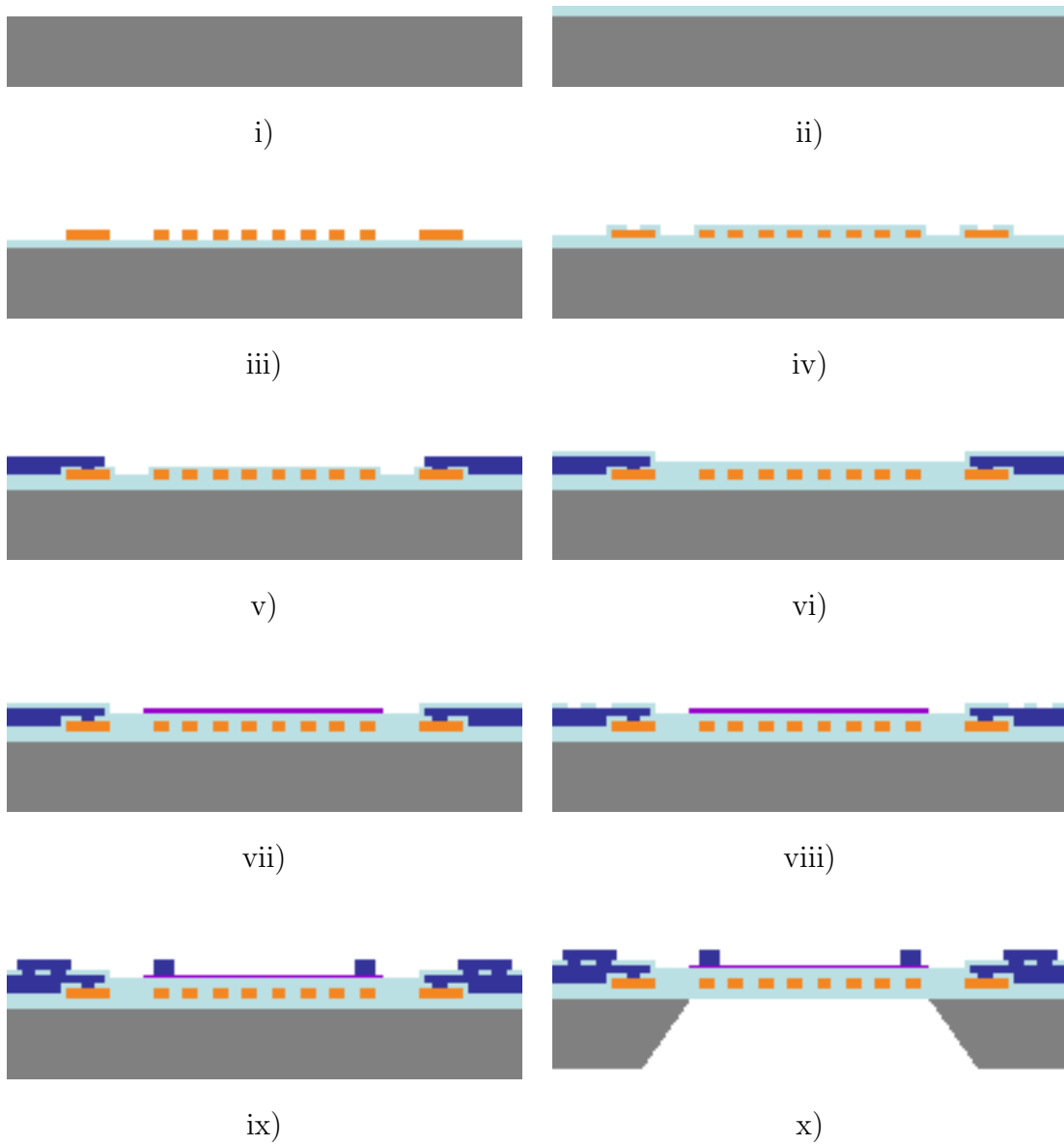


Figure 2.6: Fabrication steps of designed TiO_2 based chemical sensor

6. Portability:

The sensors should be small so that small sample volumes can be used. The power consumption should be low so that the device can be operated with a battery, making the sensor portable.

2.3.2 Sensor Arrays

Arrays of chemical sensors have been designed with the objective of improving the quantity, quality and reliability of the analytical information produced as illustrated in Fig. 2.7.

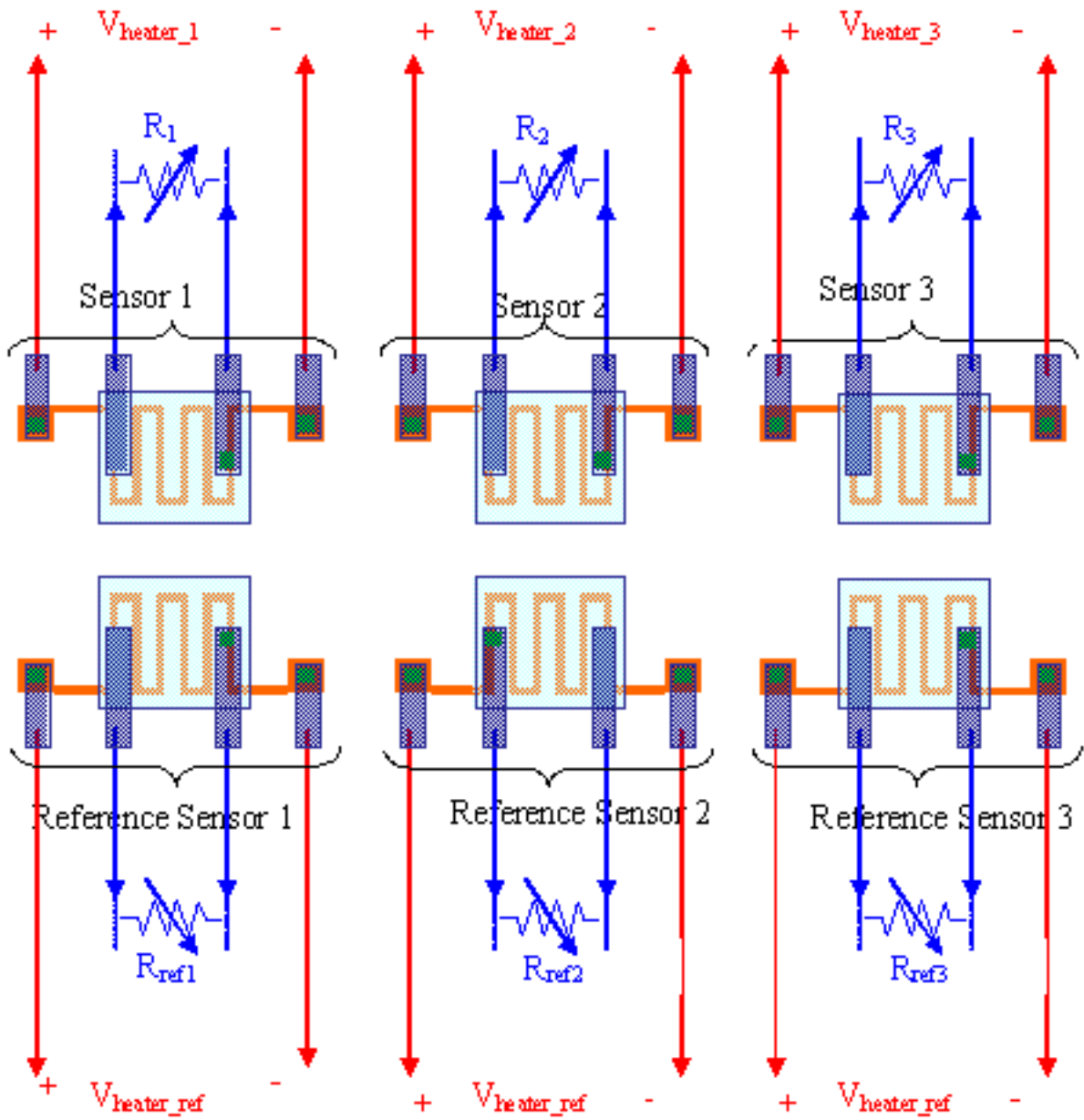


Figure 2.7: Schematic representation of sensor array

Each individual sensor, integrated with its own signal processing and conditioning circuit, is connected to a processor that takes the individual outputs and analyzes the patterns to extract analytically useful information.

CHAPTER 3

ELECTRO-THERMAL AND MECHANICAL SIMULATIONS

Reliability of the membrane structure for micromachined gas sensors is one of the main concerns in MEMS technology. The major source of this problem is the stress on the membrane. The use of $\text{SiO}_2/\text{Si}_3\text{N}_4/\text{SiO}_2$ stacked layers with optimized dimensions was found to reduce the stress on the membrane, hence improve the reliability. In this chapter, the simulation of electro-thermal characteristics and modelling of intrinsic and thermal induced mechanical stress at the membrane of the micromachined-gas sensors are presented. ANSYS [31] is used for the finite element analysis (FEA) to control mechanical stress and power consumption and also theoretical calculations for the proper selection of the membrane and heater materials.

3.1 Heat Transfer

In the simplest of terms, the discipline of heat transfer is concerned with only two things: temperature, and the flow of heat. Temperature is related to the amount of thermal energy available, whereas heat flow represents the movement of thermal energy from place to place. On a microscopic scale, thermal energy is related to the kinetic energy of molecules. The greater a material's temperature, the greater the thermal agitation of its constituent molecules (manifested both in linear motion and vibrational modes). It is natural for regions containing greater molecular kinetic energy to pass this energy to regions with less kinetic energy.

Several material properties serve to modulate the heat transferred between two regions at differing temperatures. Examples include thermal conductivities, specific heats, material densities, fluid velocities, fluid viscosities, surface emissivities, and more. Taken together, these properties serve to make the solution of many heat transfer problems a complex process.

Heat transfer mechanisms can be grouped into three broad categories; conduction, convection and radiation.

3.1.1 Conduction

Regions with greater molecular kinetic energy will pass their thermal energy to regions with less molecular energy through direct molecular collisions, a process known as conduction. In metals, a significant portion of the transported thermal energy is also carried by conduction-band electrons.

When there exist a temperature gradient within a body, heat energy will flow from the region of high temperature to the region of low temperature. This phenomenon is known as conduction heat transfer and is described in Eq. 3.1 [33]

$$q = -k \vec{\nabla} T \quad (3.1)$$

Eq. 3.1 determines the heat flux vector q , the rate of heat flowing past a reference datum, for a given temperature profile T and thermal conductivity k , a material property that describes the rate at which heat flows within a body for a given temperature difference. The minus sign ensures that heat flows down the temperature gradient.

The temperature profile within a body depends upon the rate of its internally generated heat, its capacity to store some of this heat, and its rate of thermal conduction to its boundaries (where the heat is transferred to the surrounding environment). This is stated in the Heat Equation as;

$$\vec{\nabla}^2 T - \frac{1}{\alpha} \frac{\partial T}{\partial t} = -\frac{1}{k} q_{gen} \quad (3.2)$$

along with its boundary conditions, equations that prescribe either the temperature T on, or the heat flux q through, all of the body boundaries Ω ,

$$T(\Omega_a) = T_{prescribed} \quad (3.3)$$

$$q(\Omega_b) = q_{prescribed} \quad (3.4)$$

$$\Omega_a \cup \Omega_b = \Omega \quad (3.5)$$

In the Eq. 3.2, the power generated per unit volume is expressed by q_{gen} . The thermal diffusivity α , a material property that describes the rate at which heat diffuses through a body, is related to the thermal conductivity k , the specific heat c and the density ρ by,

$$\alpha = \frac{k}{\rho c} \quad (3.6)$$

For steady state problems, the Heat Equation simplifies to,

$$\vec{\nabla}^2 T = -\frac{1}{k} q_{gen} \quad (3.7)$$

The heat equation follows from the conservation of energy for a small element within a body,

$$\begin{array}{rcccl} \text{net heat} & & \text{heat} & & \text{change in} \\ \text{conducted} & = & \text{generated} & - & \text{energy} \\ \text{out} & & \text{within} & & \text{stored within} \end{array}$$

Mathematically, this equation is expressed as,

$$\vec{\nabla} \cdot \mathbf{q} = q_{gen} - \frac{de}{dt} \quad (3.8)$$

The change in internal energy e is related to the body's ability to store heat by raising its temperature, given by,

$$\frac{de}{dt} = \rho c \frac{dT}{dt} \quad (3.9)$$

\mathbf{q} can be substituted using Eq. 3.1,

$$\vec{\nabla}(-k \vec{\nabla} T) = q_{gen} - \rho c \frac{dT}{dt} \quad (3.10)$$

$$-k \vec{\nabla}^2 T + \rho c \frac{\partial T}{\partial t} = q_{gen} \quad (3.11)$$

$$\vec{\nabla}^2 T - \frac{1}{\alpha} \frac{\partial T}{\partial t} = -\frac{1}{k} q_{gen} \quad (3.12)$$

3.1.2 Convection

When heat conducts into a static fluid it leads to a local volumetric expansion. As a result of gravity-induced pressure gradients, the expanded fluid parcel becomes buoyant and displaces, thereby transporting heat by fluid motion (i.e. convection) in addition to conduction. Such heat-induced fluid motion in initially static fluids is known as free convection. For cases where the fluid is already in motion, heat conducted into the fluid will be transported away chiefly by fluid convection. These cases, known as forced convection, require a pressure gradient to drive the fluid motion, as opposed to a gravity gradient to induce motion through buoyancy.

Heat energy transfers between a solid and a fluid when there is a temperature difference between them. This is known as “convection heat transfer”. Generally, convection heat transfer can not be ignored when there is a significant fluid motion around the solid.

The temperature of the solid due to an external field such as fluid buoyancy can induce a fluid motion. This is known as “natural convection” and it is strong function of the temperature difference between the solid and the fluid. Blowing air over the solid by using external devices such as fans and pumps can also generate a fluid motion. This is known as “forced convection” [32].

Fluid mechanics plays a major role in determining convection heat transfer. For each kind of convection heat transfer, the fluid flow can be either laminar or turbulent. Laminar flow generally occurs in relatively low velocities in a smooth laminar boundary layer over smooth small objects, while turbulent flow forms when the boundary layer is shedding or breaking due to higher velocities or rough geometries.

3.1.3 Radiation

All materials radiate thermal energy in amounts determined by their temperature, where the energy is carried by photons of light in the infrared and visible portions of the electromagnetic spectrum. When temperatures are uniform, the radiative flux between objects is in equilibrium and no net thermal energy is exchanged. The balance is upset when temperatures are not uniform, and thermal energy is transported from surfaces of higher to surfaces of lower temperature.

Radiation heat transfer is concerned with the exchange of thermal radiation energy between two or more bodies. Thermal radiation is defined as electromagnetic radiation in the wavelength range of 0.1 to 100 microns (which encompasses the visible light regime), and arises as a result of a temperature difference between two bodies.

No medium need exist between the two bodies for heat transfer to take place (as is needed by conduction and convection). Rather, the intermediaries are photons which travel at the speed of light.

The heat transferred into or out of an object by thermal radiation is a function of several components. These include its surface reflectivity, emissivity, surface area, temperature, and geometric orientation with respect to other thermally participating objects. In turn, an object's surface reflectivity and emissivity is a function of its surface conditions and composition.

3.2 Electro-thermal Behavior of Micromachined Chemical Sensors

The thermal characteristics of micromachined gas sensors have to be optimized with respect to low power consumption, well-controlled temperature distribution over the sensing layer and fast transient response.

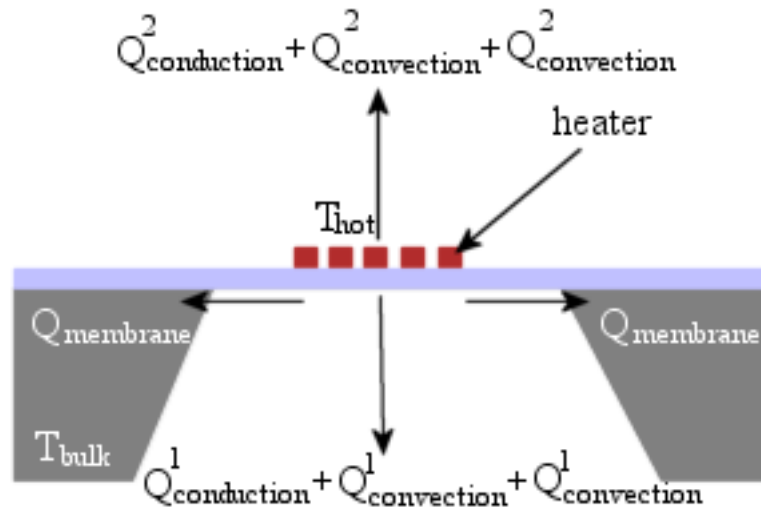


Figure 3.1: Heat fluxes of a micromachined chemical sensor

Heat transfer occurs due to heat conduction, heat convection and radiation. Above

and below the membrane heat transfer occurs due to heat conduction and heat convection through the surrounding atmosphere. In Fig. 3.1 the different flow components are shown.

Assuming that the different components of heat flow are additive, the total heat flow can be expressed as

$$Q_{tot} = G_m \cdot k_m (T_{hot} - T_{bulk}) + G_{air} \cdot k_{air} (T_{hot} - T_{bulk}) + G_{rad} \sigma \epsilon (T_{hot}^4 - T_{bulk}^4) + \Delta x \quad (3.13)$$

The first term describes the heat conduction through the closed membrane, the second the heat conduction through the ambient air, the third heat losses due to radiation and the last term accounts for unknown heat losses including free convection. G_m , G_{air} and G_{rad} are geometry factors and are empirical values which contain information about the geometry of the closed or suspended membrane and its effect on heat losses. T_{hot} and T_{bulk} denote the temperature of the hot active area and the bulk, respectively; k_m and k_{air} are the thermal conductivity of the membrane and the surrounding atmosphere; ϵ is the emissivity and σ is the Stefan-Boltzmann constant.

Numerical approximations of the temperature distribution, the total heat loss and the transient response can be obtained by replacing the sensor by a set of points which is called the computation grid or mesh. The right choice of the computational grid is very important to obtain good approximations. Increasing the number of node points results in better accuracy but leads at the same time to an increase of computational time. Therefore, it is often better to use a non-uniform grid which models the parts of the sensor which are subject to large changes with a narrow grid and regions with nearly no changes in temperature with a rather rough grid.

One way to derive the equations for the node temperatures is to divide the sensor into elements and apply the heat balance to each individual element. For each element a point i.e. the center of the element, is selected as node. Temperature and thus flow variations over the element are neglected. The node temperature is considered to be representative of the entire element.

Another possibility is to start with the differential equation, which is the mathematical description of the heat balance of an infinitesimal element, and replace the differentials by finite differences expressed in terms of the node-point temperatures. This method is known as finite-difference method.

In either case one has to solve a set of equations relating the temperature at the nodes to each other. This might get rather complicated for a large set of nodes and boundary

conditions. For this reasons ANSYS is used as a finite element analysis program to calculate the thermal behavior of the sensor system.

3.3 Mechanical Modelling of Micromachined Chemical Sensors

Micromachined chemical sensors are not only a challenge with respect to thermal design but also with respect to a mechanical design. Only by choosing the right mechanical design, following typical mistakes can be avoided:

- large intrinsic or thermal induced membrane stress leading to membrane deformation/breaking of the membrane
- deformation at the SnO_2 contact area
- deformation or breaking of the membrane due to deposition of sensing layer
- stress in the membrane

Intrinsic stress in single layer or multilayer compositions can occur due to thermal stress and residual stress [35]. Thermal induced stress is caused by mismatch in the thermal expansion coefficients of different films, which might lead to undesirable warping effects, or it is caused by non-uniform temperature distribution which might event vary in time. The latter points out that thermal design and mechanical design are strongly tied up with each other.

Thicknesses of the stacked dielectric layers comprising $SiO_2/Si_3N_4/SiO_2$ on the membrane have been optimized to reduce the intrinsic stress, which can be calculated using [36]

$$\sigma = \frac{(\sigma_1 d_1 + \sigma_2 d_2 + \sigma_3 d_3)}{d_1 + d_2 + d_3} \quad (3.14)$$

where d_i and $\sigma_{(i=1,2,3)}$ are the intrinsic stress values and thicknesses for the first oxide, nitride, and the second oxide layers, respectively. Using Eq. 3.14, we have calculated the possible thickness combinations for each layer. We used the acceptable total intrinsic stress range $-0.1GPa < \sigma < 0.1GPa$. Table 3.1 shows the calculated thickness combinations for the optimum intrinsic stress of the stack (σ values for thermal SiO_2 -0.27GPa and for LPCVD Si_3N_4 1.2GPa were used in the calculations.

Table 3.1: Stacked layer thickness vs. intrinsic pressure

SiO_2 1 st layer (μm)	Si_3N_4 2 nd layer (μm)	SiO_2 3 rd (μm) layer	Intrinsic stress (GPa)
0.5	0.2	0.4	-0.0027
0.5	0.3	0.8	-0.0056
0.8	0.2	0.1	-0.0027
0.8	0.3	0.5	0.0056
0.7	0.2	0.2	-0.0027
0.7	0.3	0.6	0.0056

3.4 Simulation Results

Some important material properties of the membrane $SiO_2/Si_3N_4/SiO_2$ and heater (polysilicon) used in the simulations are shown in Table 3.2. The power consumption of the sensor membrane could be optimized through the thermal performance of the microheater. The right selection of the heater dimensions is crucial to reduce the power consumption. Hence, the meander style heater was used in our simulations. The temperature distribution on the membrane is another key issue. It should be uniform and have high amplitude in the active area while having smaller amplitude out of the active area in order to provide a reliability and continuity for the surrounding IC circuitry. Various structural thicknesses and other parameters (such as finger spacing of the meander style heater, finger width etc.) were applied. The results are presented in Table 3.3, where A is the width of the fingers, W is the space between fingers, V is the applied voltage, Tmin is the temperature at the edges of the membrane while Tmax is the temperature in the center of the heater and Sx, Sy and Sz are the total stresses in the x, y and z direction. The membrane thicknesses are 0.8 m, 0.3 m, and 0.5 m from the top oxide to the bottom, respectively, and the heater thickness is 1 m. As seen in Table 3.3, our set of goals have been achieved with an applied voltage of 4.5 V, a finger width of 4 m and a space between fingers of 7 m. Fig. 3.2a shows the temperature distribution and Fig. 3.2 shows the stress in the z direction from the simulation. The maximum temperature and the stress, encountered at the center of the heater, are 803 K (530 C) and 0.097 GPa, respectively. Both the temperature and stress distributions confirm the

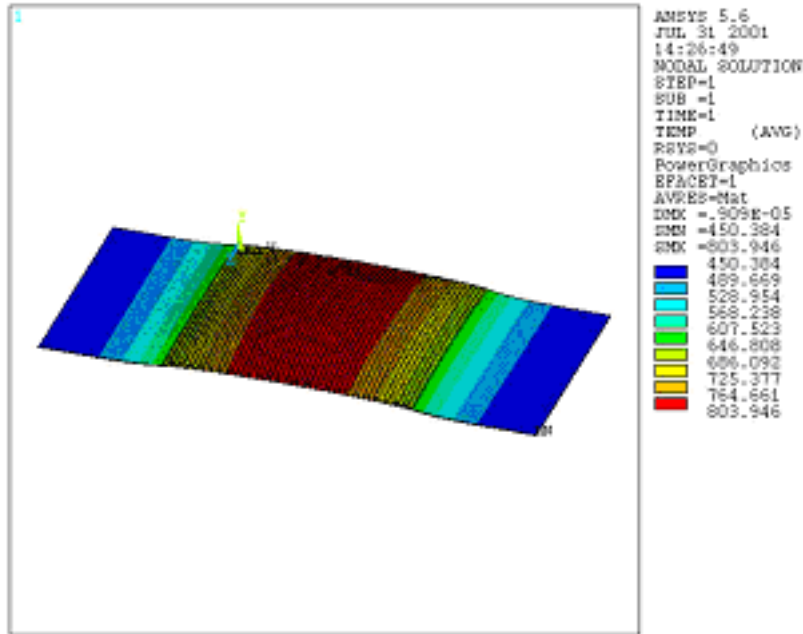
achievement of our goals by the appropriate selection of materials and structural properties.

Table 3.2: Material Properties

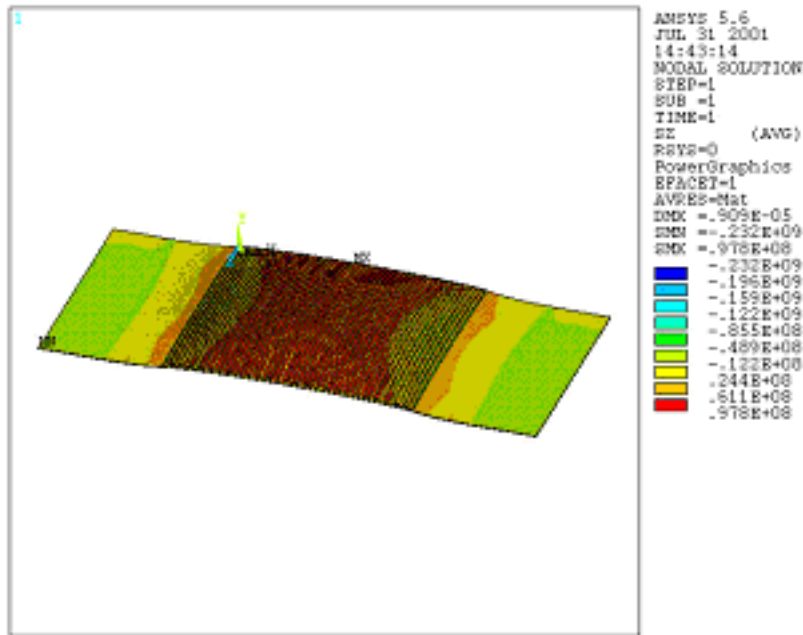
	SiO_2	Si_3N_4	Polysilicon
Young's Modulus (GPa)	67	146	150
Poisson's Ratio	0.17	0.27	0.3
Thermal Expansion Coefficient ($10^{-6}K^{-1}$)	0.4	2.8	2.33
Density (gm/cm^3)	2.3	3.0	2.33
Thermal Conductivity ($\frac{W}{m}K$)	1.4	18.5	29

Table 3.3: Simulation Results

Simulation Parameters						Simulation Results					
A μm	W μm	V μm	Number of Fingers	Active Area $\mu m \times \mu m$	Total Area $\mu m \times \mu m$	Tmin $^{\circ}C$	Tmax $^{\circ}C$	Sx GPa	Sy GPa	Sz GPa	Power Consumption mW
3.5	6	4	60	500×564	500×1064	107	326	0.075	0.036	0.072	24
3.5	6	4.5	60	500×564	500×1064	128	406	0.082	0.040	0.082	30.4
3.5	6	4.5	52	500×348	500×1188	97	497	0.096	0.050	0.093	35.1
4	7	4.5	52	500×565	500×1125	177	530	0.091	0.043	0.097	40.1
3.5	7	4.5	52	500×539	500×1519	162	480	0.089	0.043	0.091	35.1



(a)



(b)

Figure 3.2: (a) Temperature distribution on the stacked membrane. 500°C was obtained with power consumption less than 100 mW. (b) Stress distribution on the stacked membrane in the Z direction.

CHAPTER 4

DESIGN OF ELECTRONIC CIRCUITRY OF CHEMICAL SENSORS

The response of chemical sensors (e.g. resistance change) needs to be measured and converted into an analog electrical signal (e.g. a voltage) by using interface circuits. Then, this analog signal is sampled, digitized and stored in computer memory. Finally, the sampled signal is digitally pre-processed in order to make it suitable for pattern analysis.

4.1 Interface Circuits Used In Chemical Sensors

Sensor interface circuits constitute the first stage of electronic instrumentation. The purpose of these circuits is to generate an electrical signal that reflects the changes in the sensors.

4.1.1 Resistive Type Sensors

The presence of gases changes the conductivity of the sensing layer. Interface circuits for these type of sensors are, therefore, relatively simple since they only involve measuring resistance changes. Two types of resistance measurement circuits are commonly used, voltage dividers and Wheatstone bridge. In this thesis the linear version of these circuits that involve operational amplifier design is used to sense the change in the conductance of sensing layer.

4.1.1.1 Voltage Dividers

The standard method of measuring large resistance is to use voltage divider, as shown in Fig. 4.1. This circuit is very popular due to its simplicity. The resistive sensor element is placed in series with a reference sensor whose resistance is constant at a specific temperature and connected to a voltage reference V_{DC} . The current through the sensitive element and reference resistance becomes:

$$I_S = \frac{V_{DC}}{R_{sensor} + R_{ref}} \quad (4.1)$$

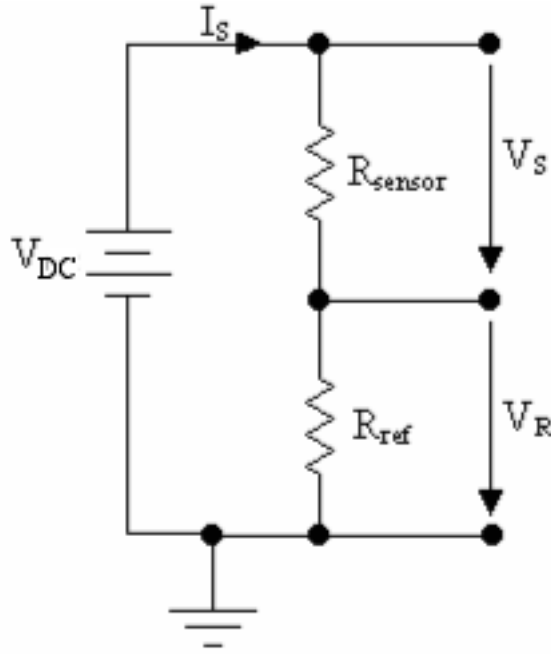


Figure 4.1: Voltage divider

Changes in sensor resistance are then measured as voltage changes across the sensor (V_S) or the reference resistor (V_R). Here, the voltage across the reference resistor is used since it is a single-ended measurement and the subsequent derivation becomes simpler. Using Ohm's Law, the resulting output voltage becomes:

$$V_R = I_S R_{ref} = \frac{V_{DC}}{R_{sensor} + R_{ref}} R_{ref} \quad (4.2)$$

The value of the reference resistor should be selected to maximize the sensitivity of the circuit, this is, the slope of the V_R - R_{sensor} curve, which can be calculated as:

$$\begin{aligned}
S = \frac{\partial V_R}{\partial R_{sensor}} &= \frac{\partial}{\partial R_{sensor}} \left(\frac{R_{ref}}{R_{ref} + R_{sensor}} V_{DC} \right) \\
&= V_{DC} \frac{-R_{ref}}{(R_{sensor} + R_{ref})^2}
\end{aligned} \tag{4.3}$$

The maximum of the sensitivity is finally determined by finding the zeros of its partial derivative with respect to R_{ref} :

$$\frac{\partial S}{\partial R_{ref}} = \frac{\partial}{\partial R_{ref}} \left(\frac{-R_{ref}}{(R_{sensor} + R_{ref})^2} V_{DC} \right) = 0 \tag{4.4}$$

$$\left(\frac{R_{ref} - R_{sensor}}{R_{ref} + R_{sensor}} \right) = 0 \tag{4.5}$$

The relationship between the sensor resistance R_{sensor} and the output voltage V_R is non-linear since the current I_s through the sensor depends not only on the reference resistor but also on the sensor resistance.

4.1.1.2 The Wheatstone Bridge

When the resistance changes to be measured are small relative to the reference sensor's resistance, the information in the output voltage will consist of small fluctuations superimposed on a large offset voltage. Although the sensitivity can be boosted with a gain stage, the problem remains since a large portion of the dynamic range of the ADC (Analog to Digital Converter) will be "wasted" in measuring the offset voltage. One solution for measuring small resistance changes is to subtract the offset voltage with a second voltage divider, as shown in Fig. 4.2. The differential voltage in the bridge is:

$$V_{out} = R_{ref} I_S - R_2 I_2 = V_{DC} \left(\frac{R_{ref}}{R_{sensor} + R_{ref}} - \frac{R_2}{R_1 + R_2} \right) \tag{4.6}$$

As in the voltage divider of Fig. 4.1, the maximum sensitivity for the Wheatstone bridge is obtained by choosing resistors R_1 , R_2 and R_{ref} equal to the sensor baseline resistance. This measurement approach is known as a deflection method, since the sensor response is measured as a differential voltage when the bridge becomes unbalanced.

The wheatstone bridge has the same sensitivity as the voltage divider. The only difference between the 4.2 and 4.6 is the offset voltage provided by the R_1 - R_2 arm, which does not

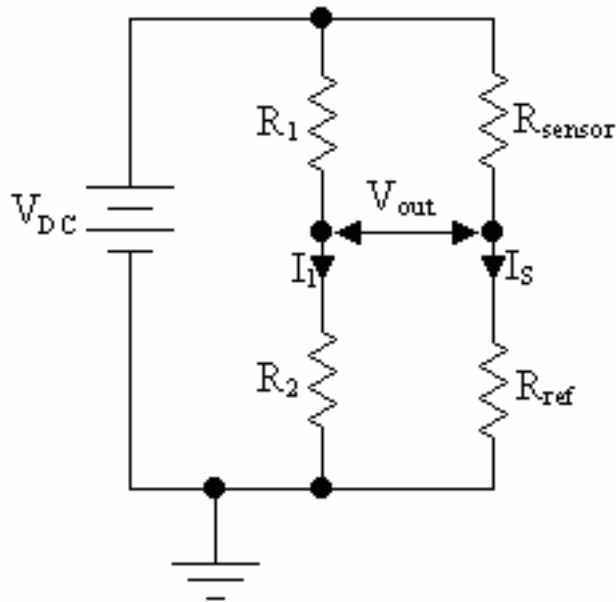


Figure 4.2: Wheatstone bridge

depend on the sensor resistance. The main advantage of the Wheatstone bridge is that it affords higher amplification gains since the offset voltage has already been removed.

4.1.2 Operational Amplifiers

Operational amplifiers are used to implement a variety of instrumentation circuits. An op-amp is essentially a high-gain amplifier that generates an output voltage $V_O = AV_{diff}$ proportional to the difference voltage V_{diff} between a non-inverting (+) and inverting (-) input and open-loop gain A . This is illustrated in Fig. 4.3 The power necessary to perform the signal amplification is derived from the supply voltages ($\pm V_S$) and, therefore, the output voltage V_{out} is constrained by $-V_S \leq V_{out} \leq V_S$. Op-amp circuits in this open-loop configuration are not practical since very small difference voltages V_{diff} will drive the output voltage to saturation. In addition, the open-loop gain (A) has a limited bandwidth because A decays significantly with frequency, and is very sensitive to temperature and power supply fluctuations. For these reasons op-amps circuits typically contain a feedback loop to control the gain as shown in Fig. 4.4.

The ideal op-amp should have following characteristics:

- i infinite open-loop gain and bandwidth $A(f) \rightarrow \infty$,

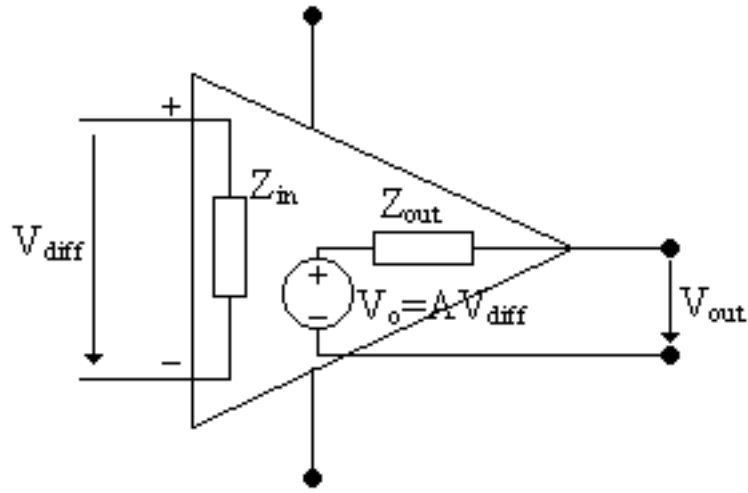


Figure 4.3: Simplified model of operational amplifiers

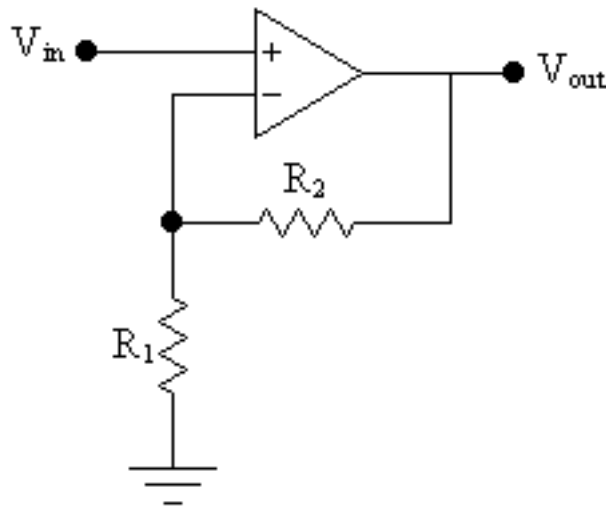


Figure 4.4: Operational amplifier having negative feedback loop

ii infinite input impedance $Z_{in} \rightarrow \infty$,

iii zero output impedance $Z_{out} = 0$

The latter implies that loading effects are negligible, this is, $V_o = V_{out}$ in the equivalent op-amp circuit of Fig. 4.3

4.2 Design of Operational Transconductance Amplifiers (OTAs)

Operational transconductance amplifier is characterized as a voltage-driven current source and in its simplest form is a combination of a differential input pair with a current mirror as shown in Fig. 4.6. This type of amplifier is a simple circuit with a relatively small chip area and has a high bandwidth and also a good common mode rejection ratio up to very high frequencies. The small signal transconductance, $g_m = \partial I_{out} / \partial V_{in}$, can be controlled by the tail current [37].

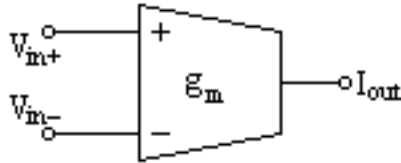


Figure 4.5: Symbol of differential input OTA

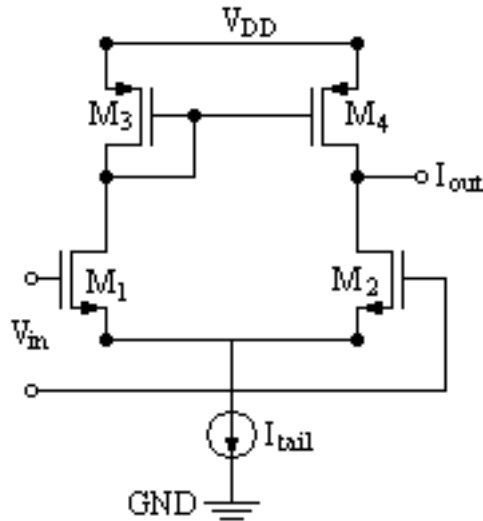


Figure 4.6: Simple differential input OTA

A CMOS OTA with an output swing much higher than that in Fig. 4.6 is shown in Fig. 4.7. This configuration needs two extra current mirrors and consumes more current, but the output voltage is, in the case when common-mode input voltage is zero, about doubled. A high voltage gain from the input nodes to the current mirror is good for reducing noise and mismatch effects; on the other hand, too much gain also reduces the upper limit of the common-mode input voltage range and the phase margin needed to ensure stability. The

frequency behavior of the OTA in Fig. 4.7 is rather complex since there are two different signal paths in parallel, as shown in Fig. 4.8. In this scheme, r_p represents the parallel value of the output resistance of the stage ($r_{o6}||r_{o8}$) and the load resistance (R_L); therefore,

$$r_p = r_{o6}||r_{o8}||R_L \quad (4.7)$$

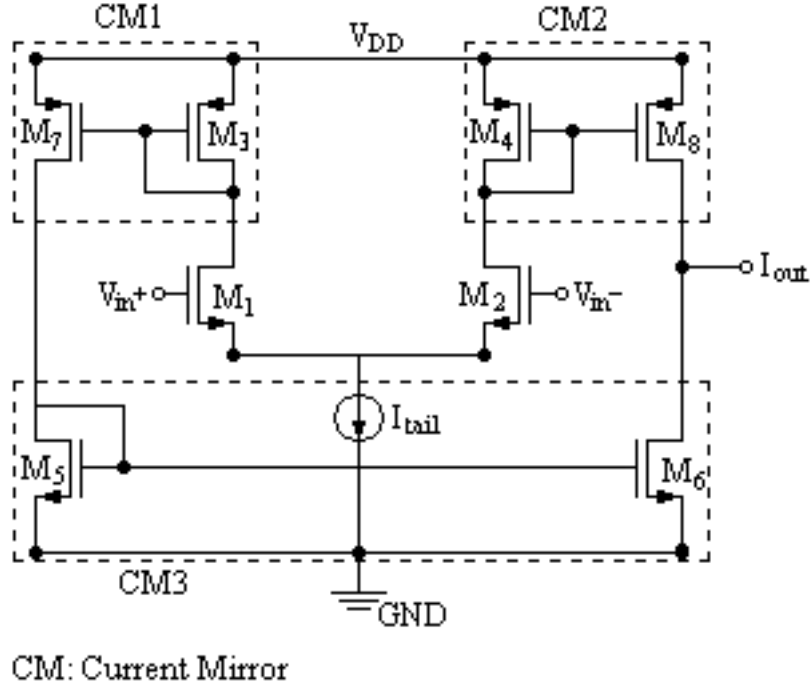


Figure 4.7: An OTA with an improved output swing

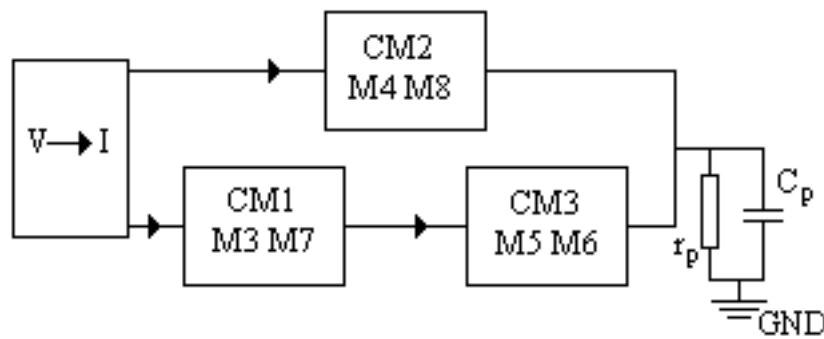


Figure 4.8: The signal paths of the OTA in Fig. 4.7

The capacitor C_p represents the sum of the parasitic output capacitance and the load capacitance $C_p = C_o + C_L$. Using the half-circuit principle for the differential pair, a fast signal path can be seen from M_2 via current mirror M_4, M_8 to the output. This signal path contributes an extra high-frequency pole. The other signal path leads from transistor M_1

via both current mirrors M_3, M_7 and M_5, M_6 to the output. In this path, two extra poles are added. The first (dominant) pole (ω_1) is determined by r_p and C_p .

$$\omega_1 = \frac{1}{r_p C_p} \quad (4.8)$$

The second pole (ω_2) is determined by the transconductance of M_3 and the sum of the gate-source capacitance of M_3 and M_4 . If M_3 and M_4 are equal, the second pole is located at:

$$\omega_2 = \frac{g_{m3}}{2C_{gs3}} \quad (4.9)$$

The unity-gain corner frequency ω_T of the loaded OTA is at:

$$\omega_T = \frac{g_{m1}}{C_p} \quad (4.10)$$

Therefore, the ratio ω_2/ω_T is:

$$\frac{\omega_2}{\omega_T} = \frac{g_{m3}}{g_{m1}} \frac{C_p}{2C_{gs3}} \quad (4.11)$$

When the OTA is used for high-frequency filter design, an integrator behavior is required, that is, a constant 90° phase at least at frequencies around ω_T . Therefore, a high value of the ratio ω_2/ω_T is needed in order to have as little influence as possible from the second pole. It is obvious from Eq. 4.10 that the low frequency voltage gain from the input nodes of the circuit to the input of the current mirrors ($= g_{m1}/g_{m3}$) must not be chosen too high.

Sometimes, OTAs are used as unity gain voltage buffers. In this case, the emphasis is put more on obtaining high open-loop voltage gain, improved output swing, and good capability to drive capacitive loads efficiently (or small resistors); its integrator behavior is of less importance.

To increase the unloaded voltage gain, cascode transistors can be added in the output stage. This greatly increases the output impedance of the OTA and hardly decreases the phase margin. The penalty that has to be paid is an additional pole in signal path and some reduction of the maximum possible output swing. This reduction can be very small if the cascode transistors are biased on the weak inversion mode. The open-loop voltage gain can be in order of 40 to 60 dB. A possible realization of such a configuration is shown in Fig. 4.9

For driving capacitive loads (or small resistors), a large available output current is necessary. In the OTA shown so far, the amount of output current available is equal twice the quiescent current (i.e., the tail current I_{tail}). In some situations, this current can be too small. One way to increase available output current is to increase the transfer ratio of the

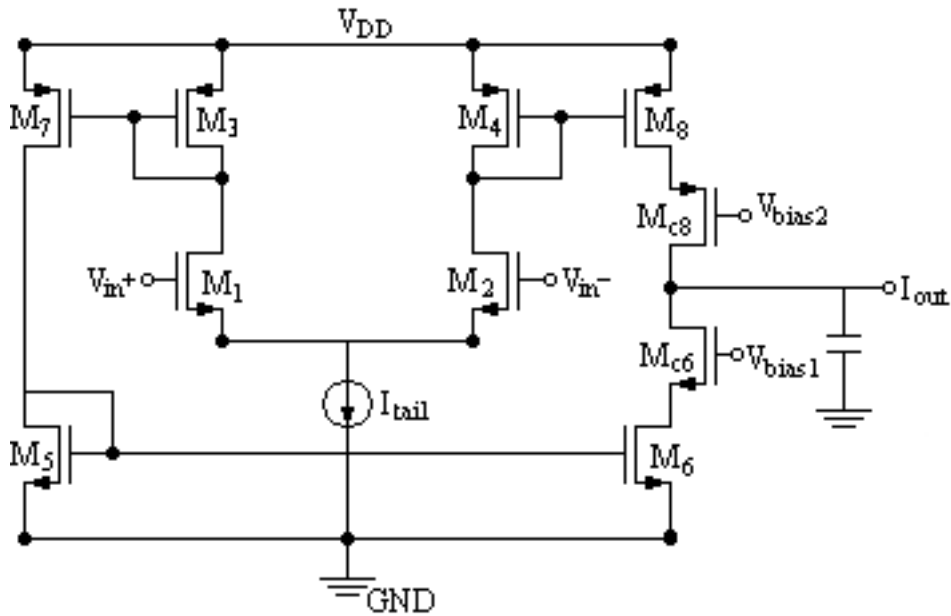


Figure 4.9: An OTA with improved output impedance

current mirrors CM1 and CM2 by a factor of B , as indicated in Fig. 4.10. The amount of available output current and also the overall transconductance increase by the same factor. Unfortunately, the -3dB frequency of the CM1 and CM2 current mirrors will be reduced by a factor $(B+1)/2$ due to the larger gate-source capacitance of the mirror output transistors. Moreover, ω_T will increase, ω_2 will decrease, and the ratio ω_2/ω_T will be strongly deteriorated. The amount of available output current through is B times the tail current. It is also possible to increase the current transfer ratio of current mirror CM3 instead of CM1. A better current efficiency then results, but at the expense of more asymmetry in the two signal paths. Although the amount of the maximum available output current is B times the tail current in both situations, the ratio between the maximum available current and tail current of the output stage remains equal to two, just as in OTAs shown in Fig. 4.7.

A CMOS inverter is used to convert the current of the output signal of OTA into voltage output as shown in Fig. 4.11.

4.3 Design of Current Mirrors

Nearly all operational amplifiers are composed of a differential pair and several current mirrors. The current mirror uses the principle that if the gate-source potential of two identi-

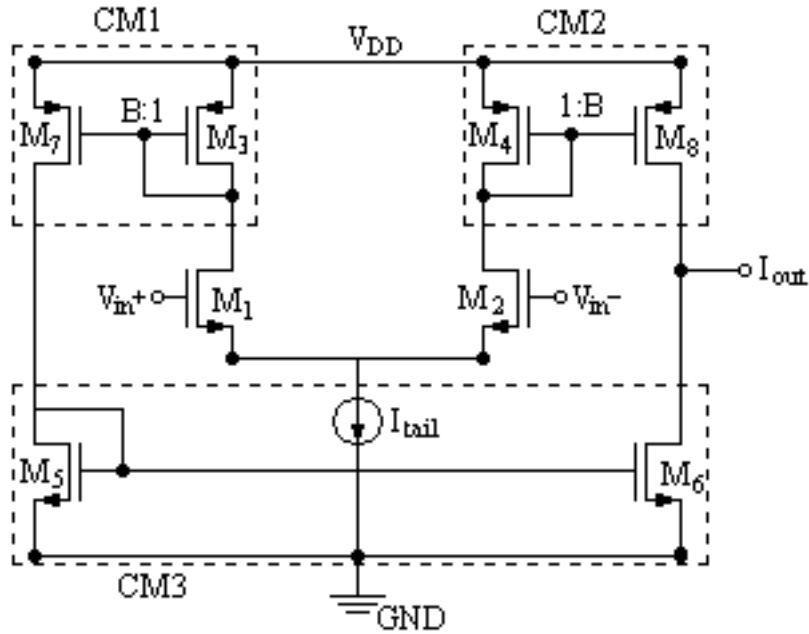


Figure 4.10: An OTA with improved load current using 1:B current mirrors.

cal MOS transistors are equal, the channel currents should be equal. Due to the continuously decreasing channel lengths and increasing usable frequency limits, some formerly usual assumptions, namely $(1/\lambda) \gg 1$ and $C_{dg} \ll C_{gs}$ are not valid any more. In this section, the basic dc and ac characteristics of current mirrors are presented.

The most frequently used current mirror is shown in Fig. 4.12.

4.3.1 DC Performance of Current Mirrors

The imperfection of the d.c current transfer ratio (B_0) resulting from unequal V_{DS} values of M_1 and M_2 is the main cause of the output off-set of OTAs and similar circuits. In order to obtain an easy to use expression for this imperfection,

$$I_D = I_{D(sat)} \frac{1 + \lambda V_{DS}}{1 + \lambda(V_{GS} - V_T)} \quad (4.12)$$

will be used which is a re-arranged form of the expression given in literature [39], where $I_{D(sat)}$ is the drain current at the saturation;

$$I_{D(sat)} = \frac{1}{2} \mu C_{ox} \frac{W}{L} (V_{GS} - V_T)^2 \quad (4.13)$$

Eq. 4.13 can be reduced to the conventional Level-1 saturation current expression,

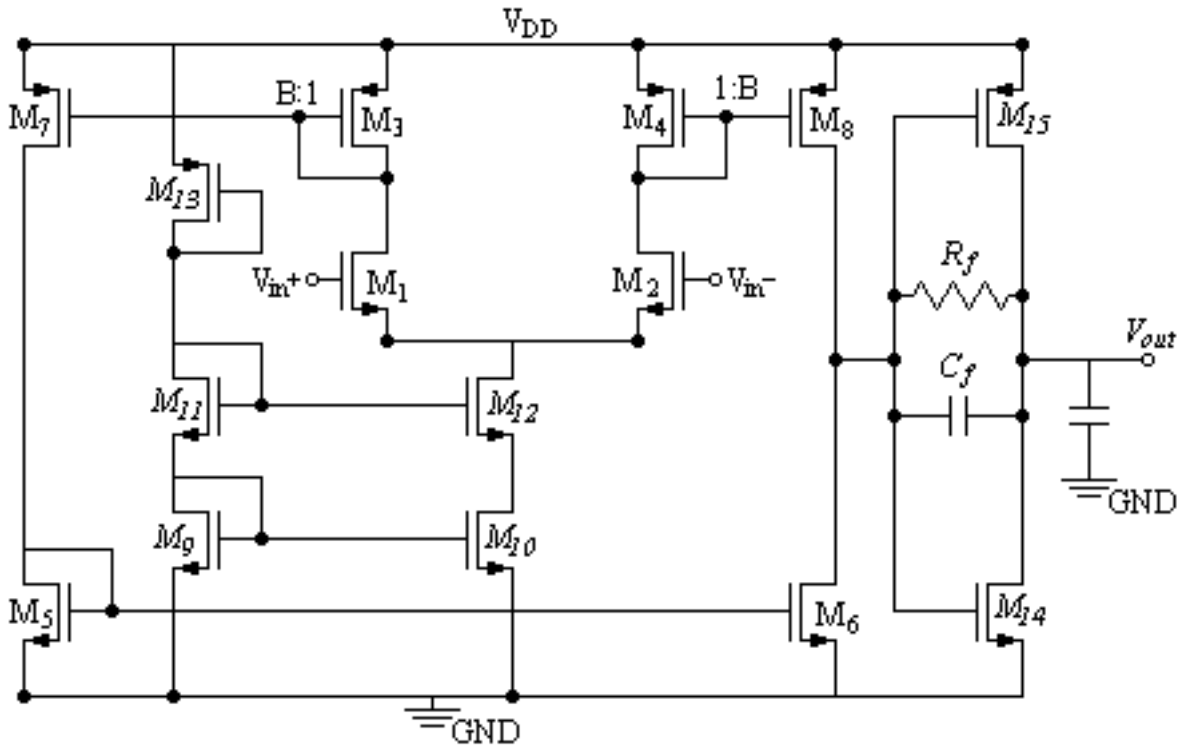


Figure 4.11: The schematic representation of OTA which is designed using AMS 0.6 μm technology

$$I_D = I_{D(sat)}(1 + \lambda V_{DS}) \quad (4.14)$$

which is valid only $\lambda(V_{GS} - V_T) \ll 1$, it means that not valid for short channel transistors.

Using Eq. 4.13 in Fig. 4.12 it is possible to calculate the W_2/W_1 for a specified B_0 and a V_{GS} , V_{DS2} set:

$$\frac{W_2}{W_1} = B_0 \frac{1 + \lambda V_{DS1}}{1 + \lambda V_{DS2}} = B_0 \frac{1 + \lambda V_{GS}}{1 + \lambda V_{DS2}} \quad (4.15)$$

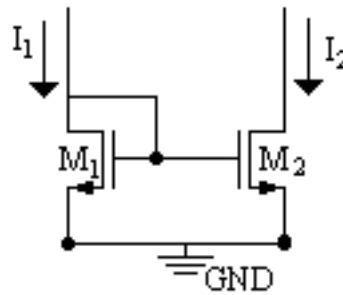


Figure 4.12: N-channel current mirror

4.3.2 AC Performance of Current Mirrors

The small signal a.c. performance of a current mirror must be characterized with its short circuit transfer ratio (B) and the output internal admittance (y_0). The small signal equivalent circuit of the basic current mirror is shown in Fig. 4.13a. To calculate the current transfer ratio and the output conductance, a modified form of the Miller theorem shown in Fig. 4.13b will be applied as in Fig. 4.13c. This approach permits to solve the circuit without any systematic error, i.e. without using the voltage gain V_B/V_A which has usually has to be calculated with certain approximations. The obtained current transfer ratio is

$$B = B_0 \frac{s_{p2}(s - s_{z2})}{s_{z2}(s - s_{p2})} \quad (4.16)$$

where B_0 is the d.c. value of the current transfer ratio, and the pole and zero

$$s_p = -\frac{g_{m1}}{C_{iT}}, \quad s_z = \frac{g_{m2}}{C_{dg2}} \quad (4.17)$$

Although the zero corresponds to a considerably higher frequency compared to the pole, it is not negligible since it is in the right half-plane and can affect the phase characteristic at high frequencies.

It is useful to calculate the value of the dominant pole, which defines the bandwidth of the mirror, in terms of physical parameters of M1 and M2, and the current:

$$s_p = -\frac{3}{\sqrt{2}} \frac{1}{(B_0 \frac{L_2}{L_1} + 1)} \frac{1}{L_1^{3/2}} \sqrt{\frac{I_1 \mu}{W_1 C_{ox}}} \quad (4.18)$$

This expression gives several valuable hints for design:

- Pole is proportional with the square root of the mobility; consequently NMOS current mirrors have considerably higher bandwidth.
- Pole has inverse proportionality with $L_1^{3/2}$ and $W_1^{1/2}$. If there is no other restriction, minimum geometry must be used for M1
- If there is no restriction for L_2 (for example to obtain a lower output conductance), minimum geometry must be used for higher bandwidth

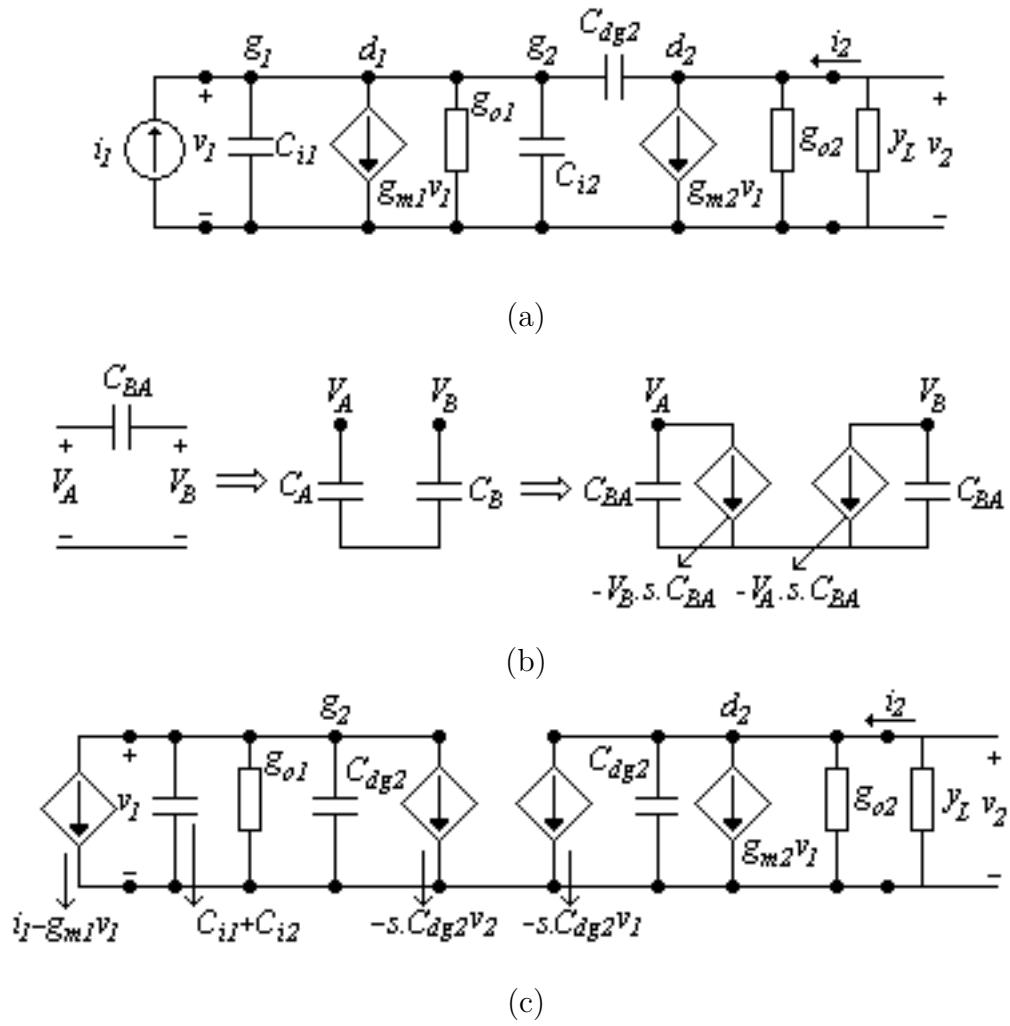


Figure 4.13: Small signal model of current mirror shown in simple N-channel current mirror

- The value of pole decreases with B_0
- The bandwidth increases with the square root of the reference current, I_1 .

The output admittance calculated from Fig. 4.13c is

$$y_0 = \frac{sC_{dg2}(g_{m2} - sC_{dg2})}{g_{m1} + g_{o1} + sC_{iT}} + g_{o2} + sC_{dg2} \quad (4.19)$$

This expression can be simplified for $g_{m2} \gg sC_{dg2}$ (means for frequencies lower than the zero frequency) and for $g_{gm1} \gg g_{o1}$ which can be shown that is valid if

$$(V_{GS} - V_T)/2(1/\lambda + V_{DS}) \ll 1 \quad (4.20)$$

and the output conductance becomes

$$y_0 \cong \frac{sC_{dg2}g_{m2}}{g_{m1} + sC_{iT}} + g_{o2} + sC_{dg2} \quad (4.21)$$

According to Eq. 4.21 the output side of the current mirror can be modelled as shown in

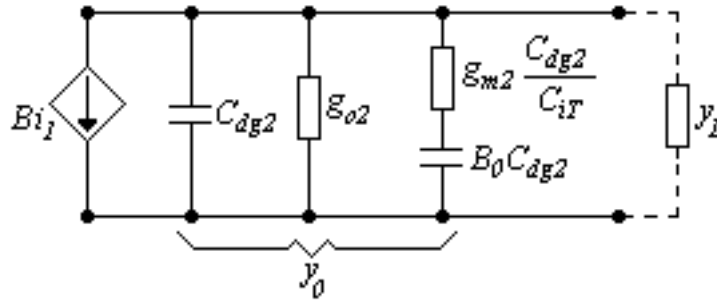


Figure 4.14: The small-signal equivalent circuit of the output of the basic current mirror

Fig. 4.14. It is obvious that Eq. 4.16 is valid only for load admittances very high compared to y_0 . Otherwise the output current (or output voltage) must be calculated from Fig. 4.14.

4.3.3 Application to Conventional Symmetrical OTA

The OTA shown in Fig. 4.10 has 3 current mirrors on the signal path, namely (M3-M7), (M4-M8), and (M5-M6). If the magnitude of the load admittance y_L is considerably higher than the output internal admittances of (M4-M8) and (M5-M6) in the interested frequency band, the transconductance of OTA can be expressed as:

$$G_m = \frac{i_o}{v_{id}} = \frac{1}{2}g_{m1}B_1(1 + B_2) \quad (4.22)$$

where g_{m1} is the transconductance of the input transistors, B_1 is the current transfer ratio of identical (M3- M7) and (M4-M8) mirrors and B_2 , having a d.c. value equal to unity, is the current transfer ratio of (M5-M6) mirror. Using Eq. 4.16 for $B - 1$ and B_2 , G_m can be re-written as:

$$G_m = \frac{1}{2}g_{m1}B_{01} \frac{s_{p1}}{s_{z1}} \frac{(s - s_{z1})(s - 2s_{p2})}{(s - s_{p1})(s - s_{p2})} \quad (4.23)$$

This gain function having two zeros (one of them in the right half-plane) and two poles has a fluctuating phase characteristic and consequently is a potential source of problems if the OTA is in a feedback loop.

4.3.4 Current Mirror Design Used in the Tail of OTA

The V_{DS2} versus I_2 curves for different V_{GS} values of the current mirror illustrated in Fig. 4.12 is shown in Fig. 4.15. Here, it is easily seen that the channel length modulation effects (λ) of the transistors cause the output current (I_2) to change in the saturation region. To improve the current-mirror performance, the circuit configuration can be modified as shown in Fig. 4.16

If all of the transistors are identical in Fig. 4.16 then the voltage on the drain of M1 is equal to that on M2. If the drain voltage of M4 is increased, then the current in M4 tries to increase. This will increase the current in M2 (decreasing V_{GS4}). Transistor M4 will begin to turn off in order to compensate for the increase in current. The result is a small decrease in V_{GS4} which causes a small increase in V_{DS2} . The resulting change in V_{DS2} is much smaller than the change in drain voltage of M4. Thus current mirroring is achieved with only a slight error due to the output-resistance effect.

Fig. 4.17 shows an equivalent small signal model of Fig. 4.16. Since, $i_1 = 0$, the small signal voltages v_1 and v_3 are both zero. Therefore, the output resistance of the cascoded current mirror will be;

$$r_{out} = r_{ds2} + r_{ds4} + g_{m4}r_{ds2}r_{ds4}(1 + g_{mbs}/g_{m4}) \quad (4.24)$$

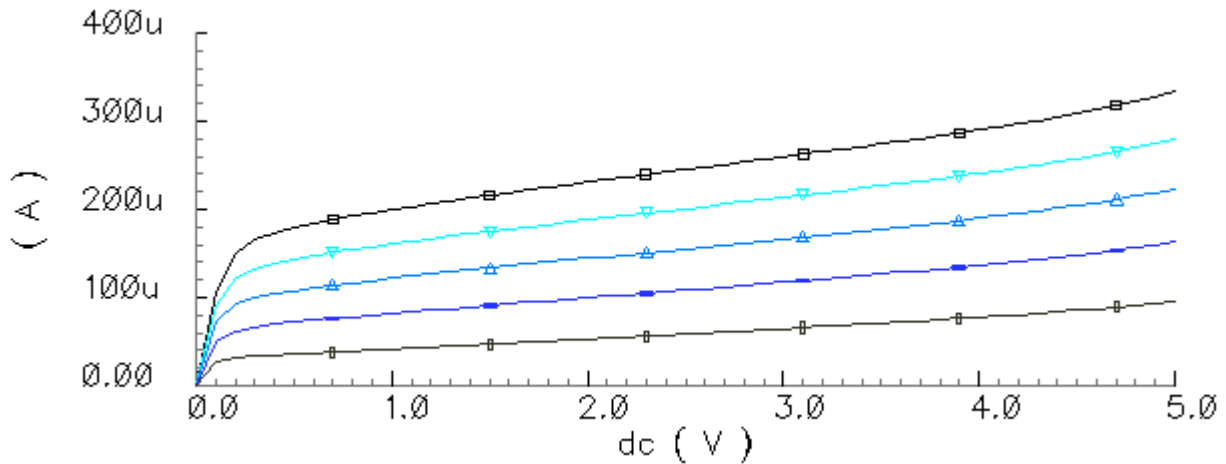


Figure 4.15: I_2 vs V_{DS2} curves

Same simulations were done to show the performance improvement of the cascoded current mirror structure. The simulation result is given in Fig. 4.18. The current voltage is nearly constant when the transistors are in saturation region, but on the other hand the

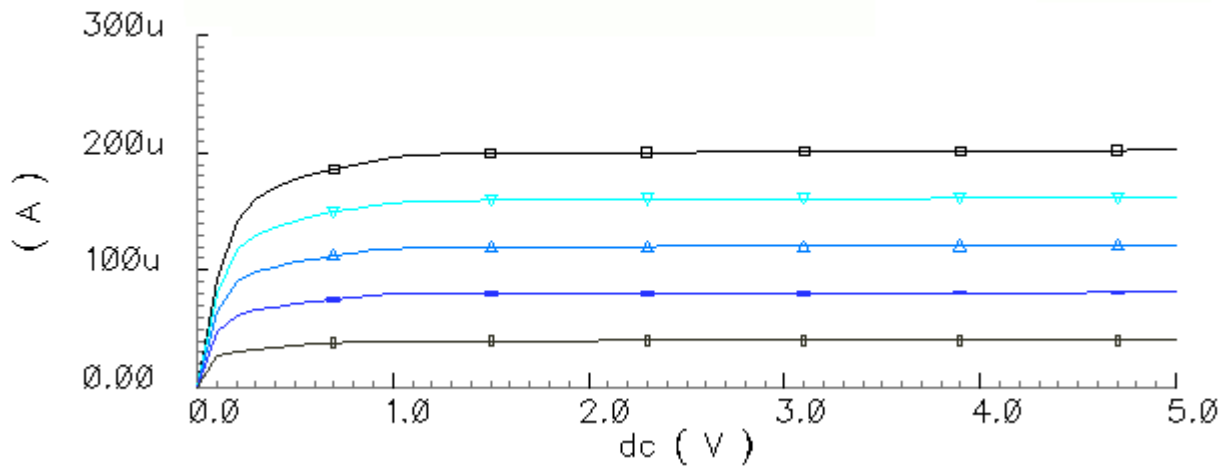


Figure 4.18: I_2 vs V_{DS2} curves for cascoded current mirror

The AC and transient open and closed-loop simulation results are shown in Fig. 4.19 to Fig. 4.25. According to these results, the open-loop bandwidth of the opamp is approximately 23 MHz and the gain at low frequencies is 41.7 dB.

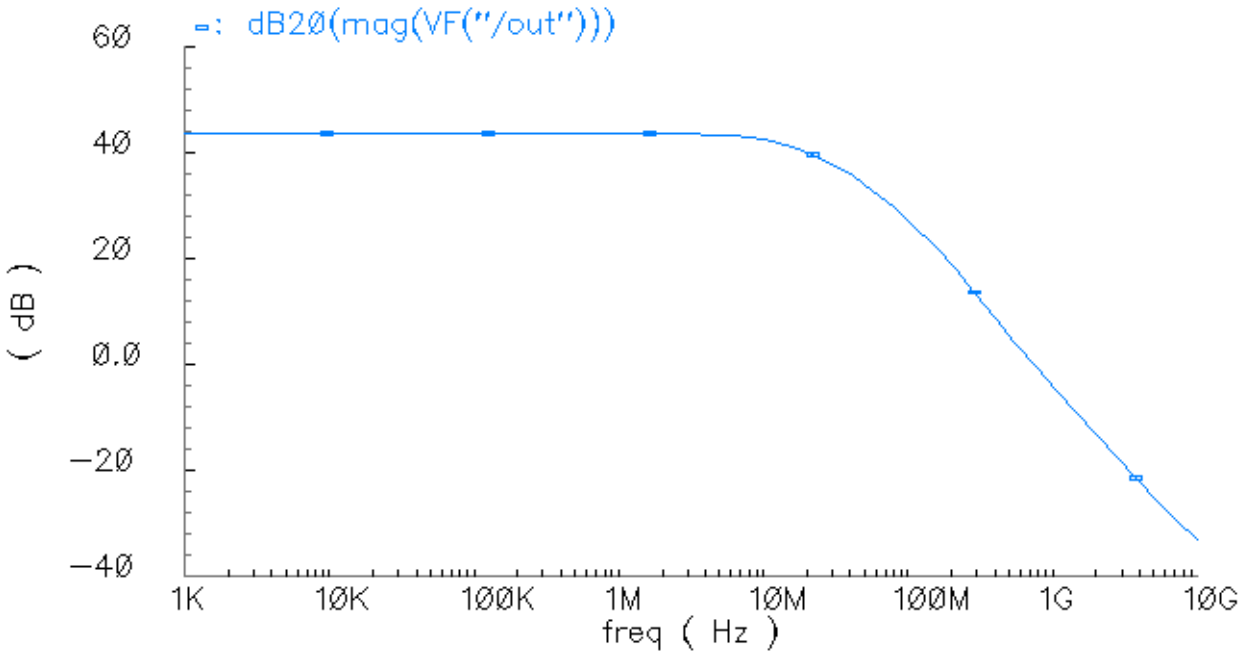


Figure 4.19: Open-loop AC characteristic of OTA: Gain at low frequencies: 41.7 dB, bandwidth: 23 MHz., Gain \times Bandwidth: 700 MHz.

Table 4.1: Dimensions of the elements used in the design of OTA

	W(μm)	L(μm)
M1	25	0.6
M2	25	0.6
M3	0.8	0.6
M4	0.8	0.6
M5	8.4	0.6
M6	8.4	0.6
M7	20	0.6
M8	20	0.6
M9	20	0.6
M10	20	0.6
M11	20	0.6
M12	20	0.6
M13	1	1
M14	8.4	0.6
M15	20	0.6
R_f	75 k Ω	
C_f	300 nF	

4.5 Integration of the Operational Amplifier and Chemical Sensor

To sense the changes in the chemical sensor's metal oxide when the gas to be detected is in a reaction with the sensor, the structure defined in Fig. 4.26 is used. In this case, the second stage is used to amplify the first stage-output by a factor of 3. That is, the slope of V_{out} will be 3 times greater than that of V_{out1} . It is important to note that the output is linearly proportional with the sensor's resistance which is the main advantage of this configuration. Furthermore, the output depends not on the reference sensor's resistance individually but on the ratio of R_{sensor} to R_{ref} . That means it is not important to know the exact value of reference sensor but to know the ratio between them.

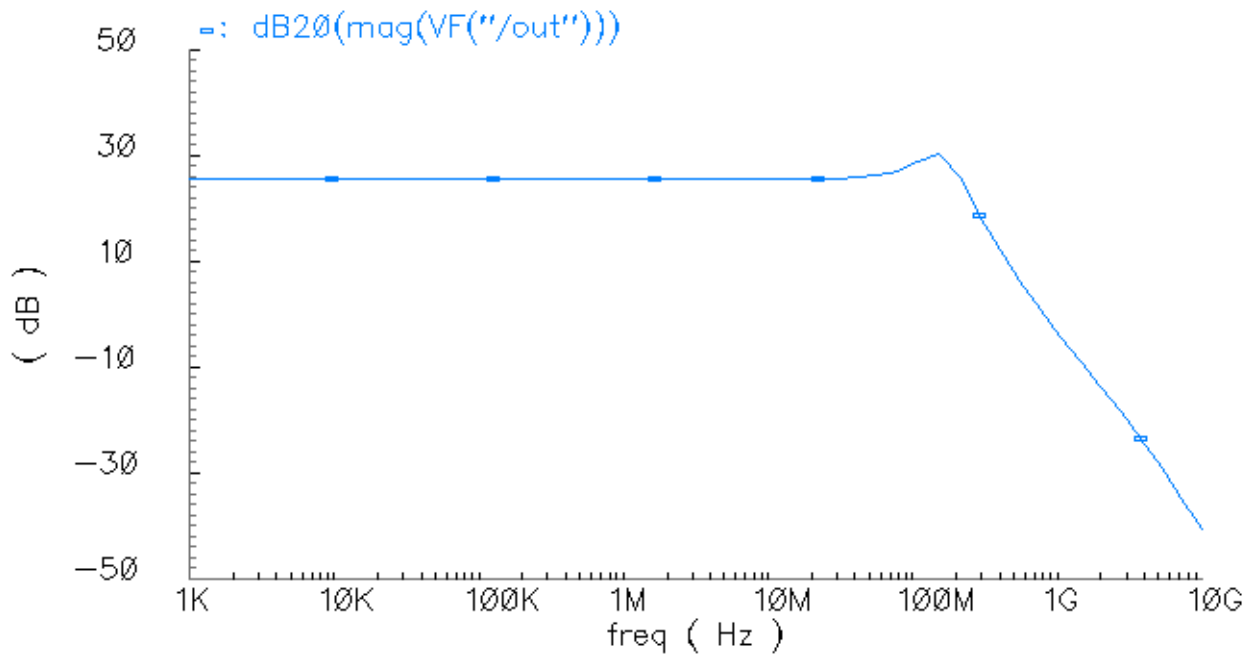


Figure 4.20: Negative feedback inverting type closed-loop AC characteristic of OTA: 700 MHz.

$$V_{out1} = 2 \left(\frac{R_{sensor}}{R_{ref}} + 1 \right) \quad (4.25)$$

$$V_{out} = 3V_{out1} - 8 \quad (4.26)$$

$$V_{out} = 2 \left(3 \frac{R_{sensor}}{R_{ref}} - 1 \right) \quad (4.27)$$

The reference sensor's resistance used in the simulations is estimated to be approximately $2M\Omega$. Also, it is assumed that the sensor resistance changes between $700k\Omega$ and $2M\Omega$. Fig. 4.27 shows the ideal response of Fig. 4.26 while Fig. 4.28 shows the simulation results of Fig. 4.26 in the Cadence environment. These results shows that when the sensor's resistance is less than $2/3M\Omega$ then the output voltage of the system shown in Fig. 4.26 is ideally at '0' voltage but in reality it is the minimum output voltage which is approximately .2 V. The reason behind this is that the amplifier's output cannot be less than 0 voltage because of the supply voltages' range ($V_{DD} = 5V$ whereas $V_{SS} = 0$).

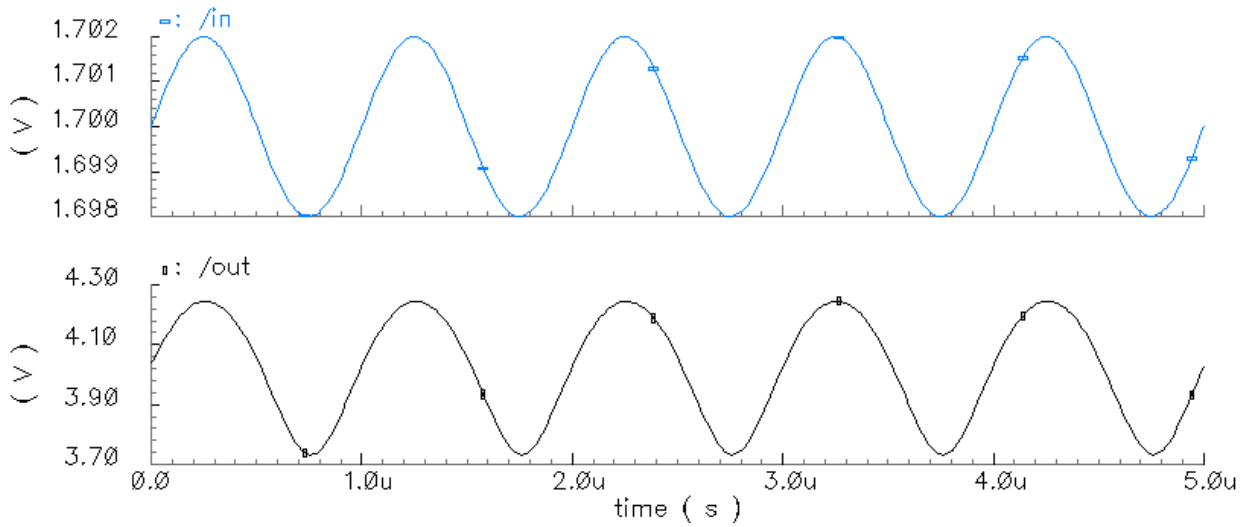


Figure 4.21: Transient response of OTA when 1 MHz sinusoidal source is applied to the differential input

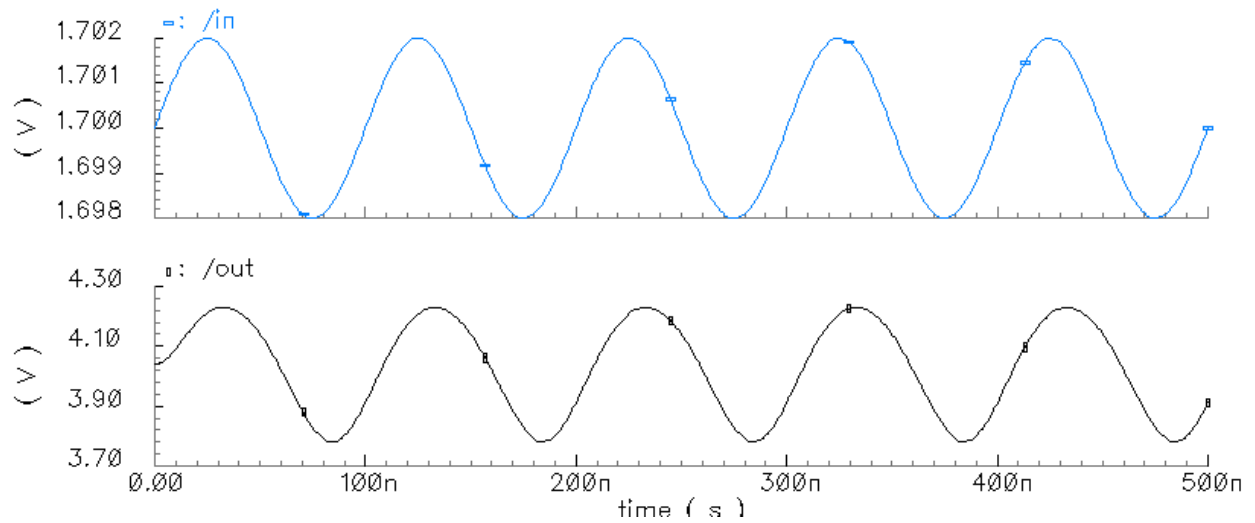


Figure 4.22: Transient response of OTA when 10 MHz sinusoidal source is applied to the differential input

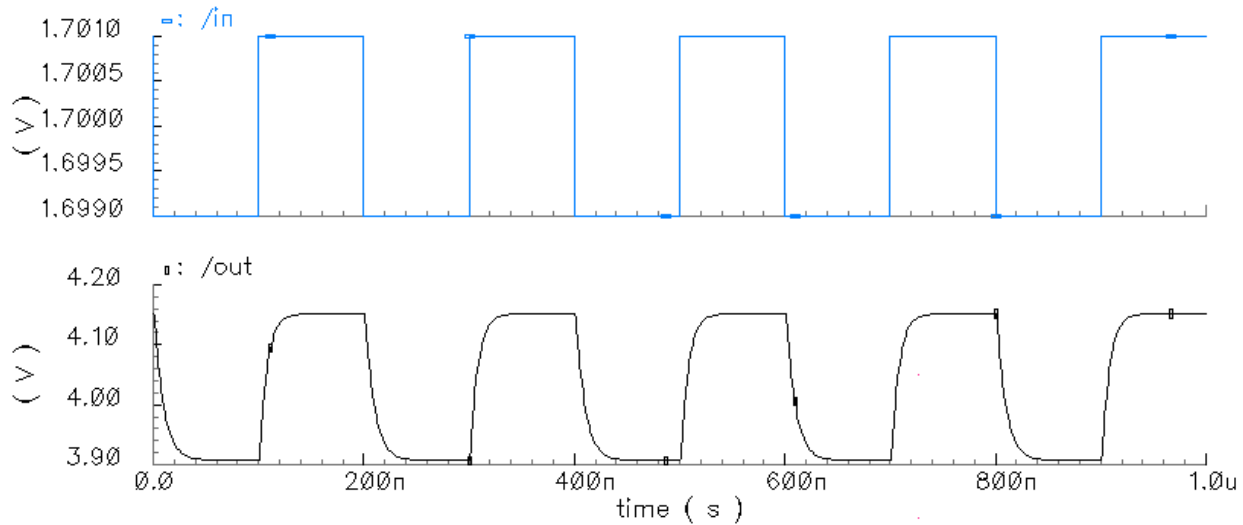


Figure 4.23: Transient response of OTA when 5 MHz pulse is applied to the differential input

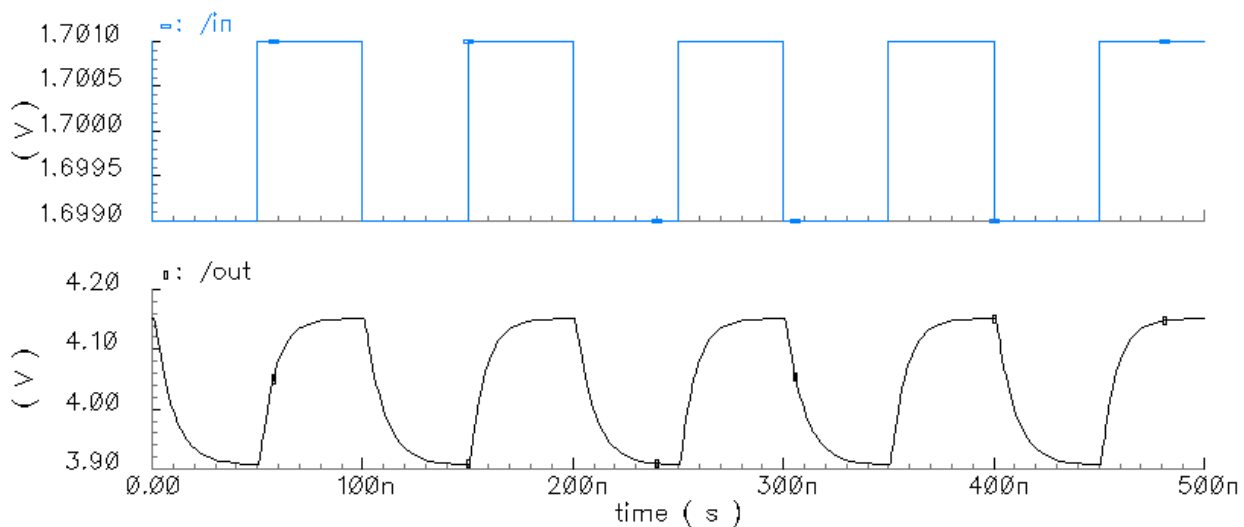


Figure 4.24: Transient response of OTA when 10 MHz pulse is applied to the differential input

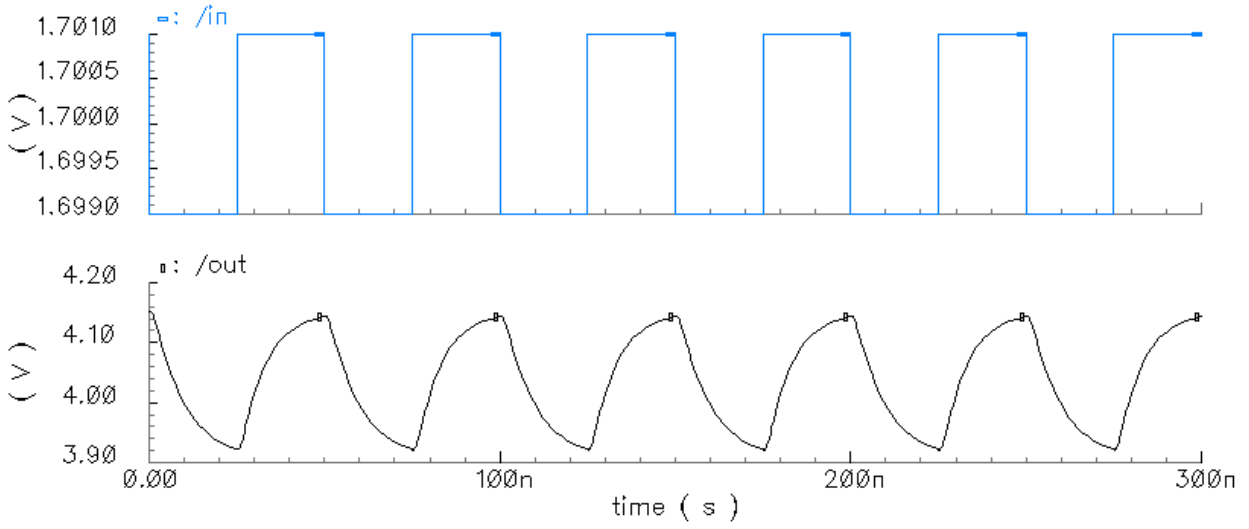


Figure 4.25: Transient response of OTA when 20 MHz pulse is applied to the differential input

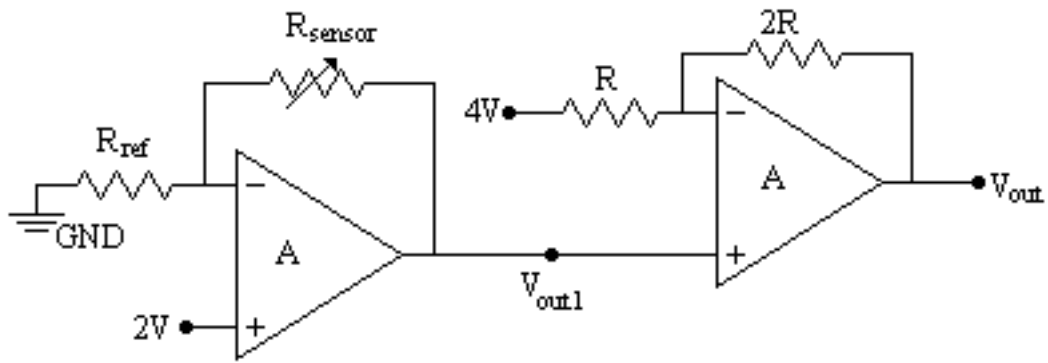


Figure 4.26: Two-stage negative feedback op-amp circuitry for gas sensing

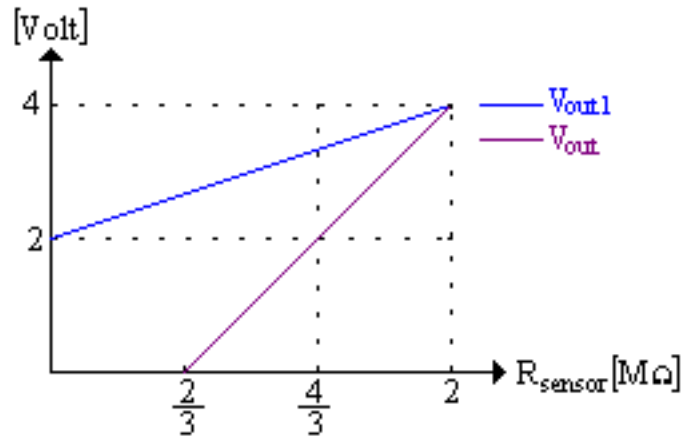


Figure 4.27: Ideal response of Fig. 4.26

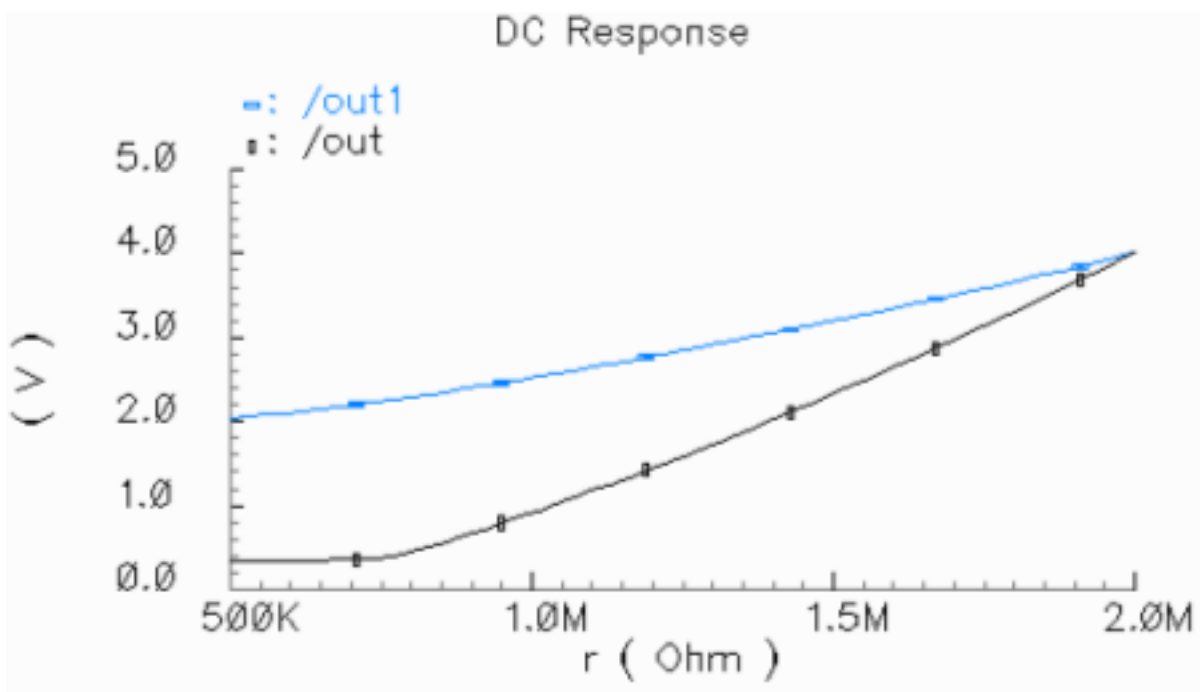


Figure 4.28: Simulation results of Fig. 4.26

CHAPTER 5

CONCLUSIONS AND FUTURE WORK

In this thesis, we designed array type micromachined chemical sensor and its electronic circuitry for detection of combustible gas species. The fabrication of the sensors should be based on the IC manufacturing technology in order to achieve the chemical sensors and electronic circuitry on the same chip. Therefore, micromachining technology, offering lower unit cost through batch production of wafers, smaller device size, better reproducibility, superior signal conditioning via less noise generated in the transmission of the sensor signals to the processing electronics, and an improved detection for the whole sensing system, was used for the realization of the sensor system.

In our design the outputs of the chemical sensors are the resistance changes occurring on the top layer, metal-oxide (TiO_2) layer, of the system. These resistance changes converted into the voltage signals by using the circuit topology explained in the previous chapter. The most important issue of this circuitry is that the output of the circuit should respond linearly to the resistance changes. For these reason the interface circuit shown in Fig. 4.26 is integrated with the chemical sensor array.

Current State and Future Work

The fabrication of the sensors has not been completed yet. There are two more masks left to be processed. Meanwhile, the interface circuitry of the sensors sent to AMS foundry will be tested. After that, these discrete parts of the sensors will be integrated and tested.

The designed systems would not be enough to sense gaseous mixtures. In this work we targeted to convert the output of the sensors into an analog signal. To identify and find the concentration levels of the mixtures, these analog signals should be converted to digital

signal and then pattern recognition algorithms should be used for the identification of the gas species. After all of the integration is finished, the “smart sensor system” will be realized.

APPENDIX A

MAXIMUM ALLOWABLE CONCENTRATIONS OF COMBUSTIBLE GASES

Table A.1: Threshold Limit Values (Maximum allowable concentrations)

Substance	Recommended Value (ppm)
acetaldehyde	200
acetone	1000
acrylonitrile	20
ammonia	50
aniline	5
benzene	25
boron trifluoride	1
bromine	0.1
butylamine	5
carbon dioxide	5000
carbon disulphide	20
carbon monoxide	50
carbon tetrachloride	10
chlorine	1
chlorine dioxide	0.1
chlorine trifluoride	0.1
cyclohexanone	50
diborane	0.1
dichloroethane	50
ethylene oxide	50
fluorine	0.1
formaldehyde	5
hexane	500
hydrogen chloride	5
hydrogen cyanide	10
hydrogen fluoride	4
hydrogen sulphide	10

Substance	Recommended Value (ppm)
lead	0.2 mg/m ³
mercury	0.1 mg/m ³
mercury (organic compounds)	0.01 mg/m ³
methyl alcohol	200
methyl bromide	20
nickel carbonyl	0.001
nitrogen dioxide	5
nitrotoluene	5
oxygen difluoride	0.05
ozone	0.1
phosgene	0.1
phosphine	0.3
pyridine	5
sulphur dioxide	5
toluene	200
trichloroethylene	100
xylene	200

APPENDIX B

DETAILED FABRICATION STEPS OF CHEMICAL SENSOR

(100) oriented double polished p-type silicon substrate



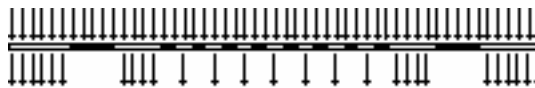
SiO_2/Si_3N_4 deposition (thickness: $0.6 + 0.25 \mu m$)



Polysilicon deposition (thickness: $1 \mu m$)



Photoresist deposition



Photoresist exposure with UV light



Polysilicon etching



Photoresist removing



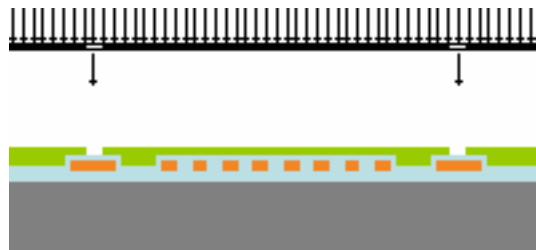
Si_3N_4 deposition (thickness:0.4 nm)



Photoresist deposition



Photoresist exposure with UV light



Si_3N_4 etching



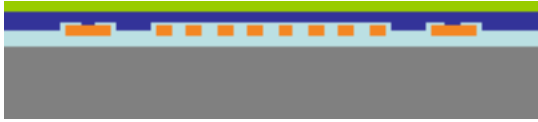
Photoresist removing



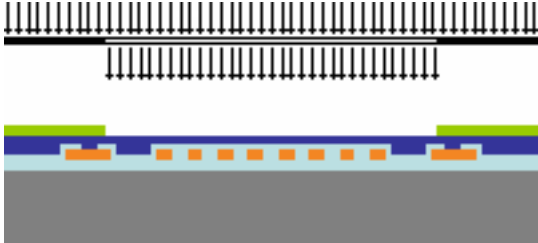
Metal 1 deposition



Photoresist deposition



Photoresist exposure



Metal 1 etching



Photoresist removing



SiO_2 deposition



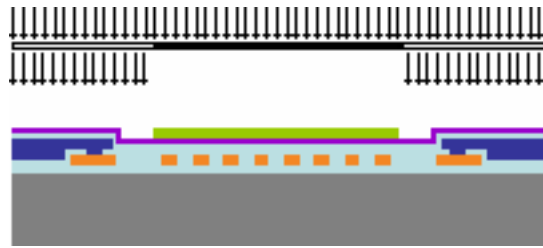
TiO_2 deposition



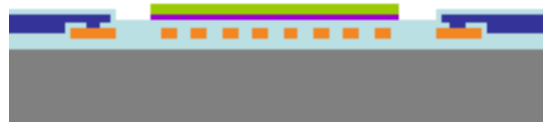
Photoresist deposition



Photoresist exposure



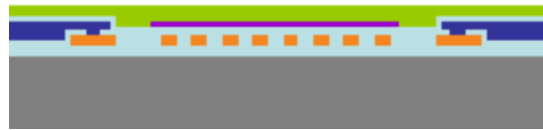
TiO_2 etching



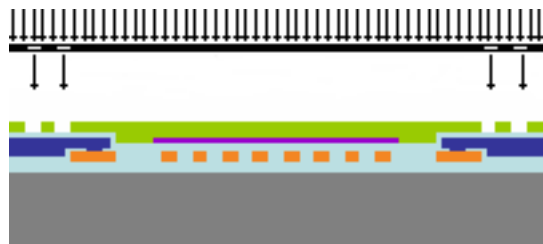
Photoresist removing



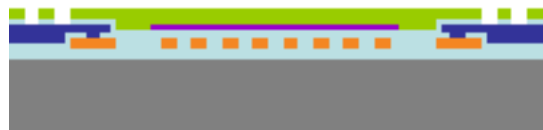
Photoresist deposition



Photoresist exposure



SiO_2 etching



Photoresist removing



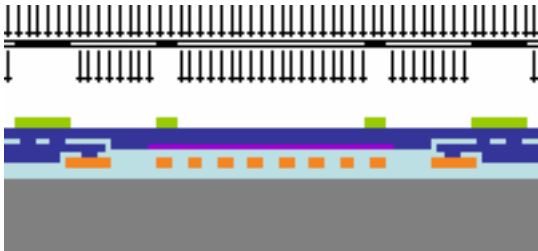
Metal 2 deposition



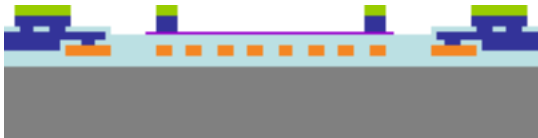
Photoresist deposition



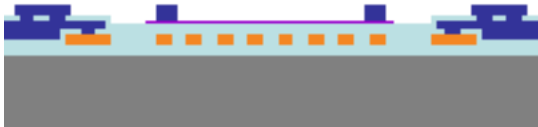
Photoresist exposure



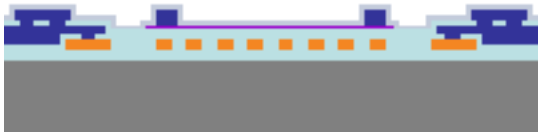
Metal 2 etching



Photoresist removing



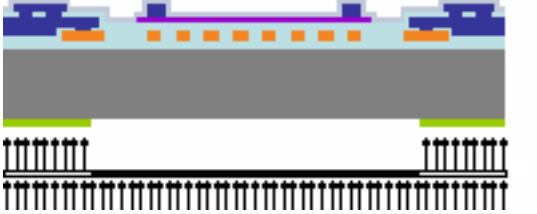
Passivation layer deposition (LTO Low Temperature Oxide)



Photoresist deposition



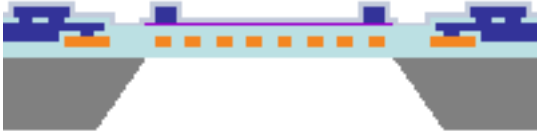
Photoresist exposure



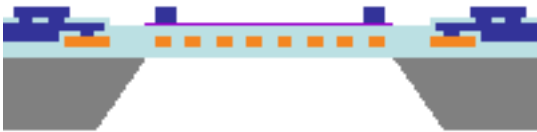
Back side etching



Photoresist removing



Removing passivation layer



APPENDIX C

MASK LAYOUTs OF CHEMICAL SENSORS AND ITS INTERFACE CIRCUITRY

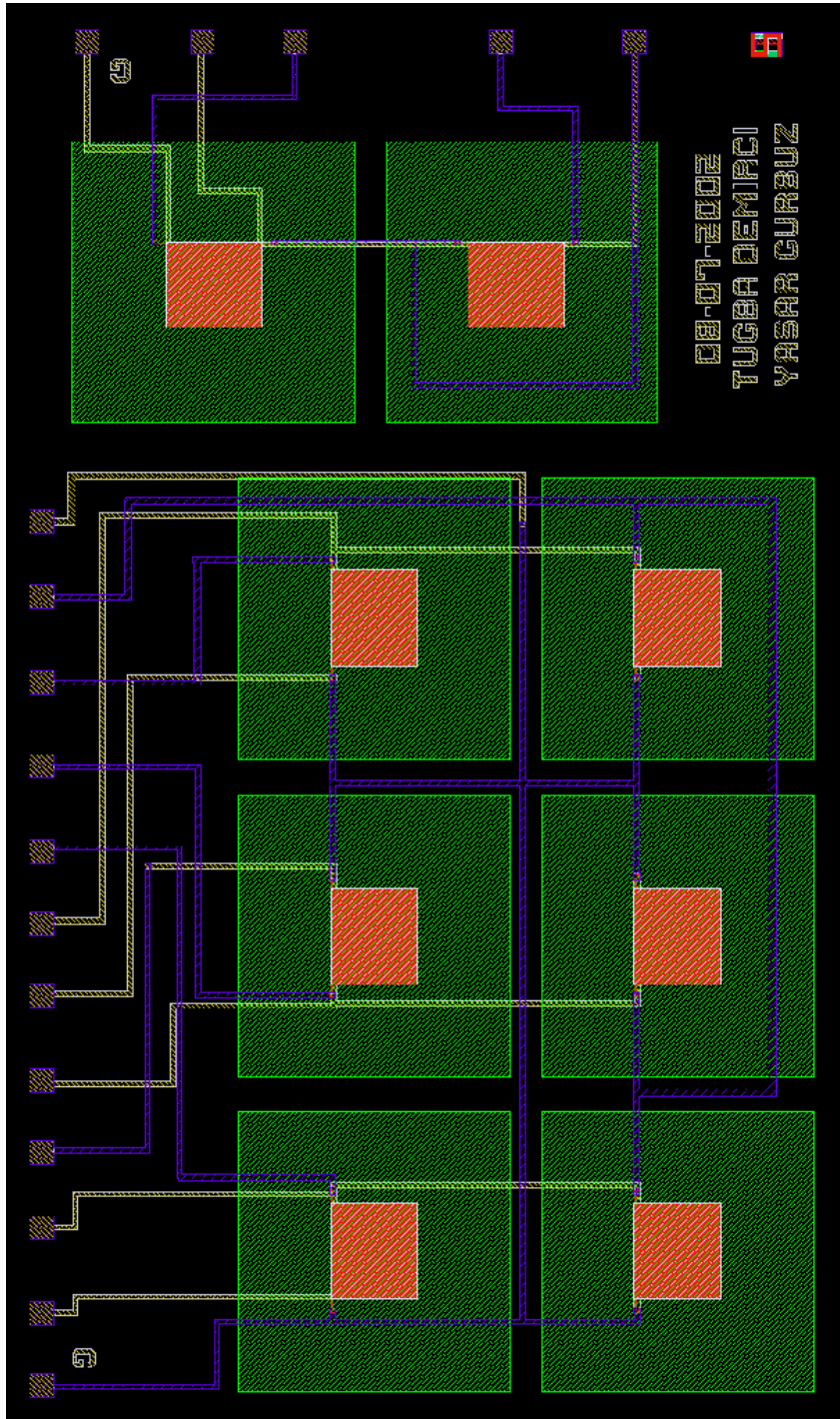


Figure C.1: Mask layout of 3x2 sensor system and 2x1 test sensor

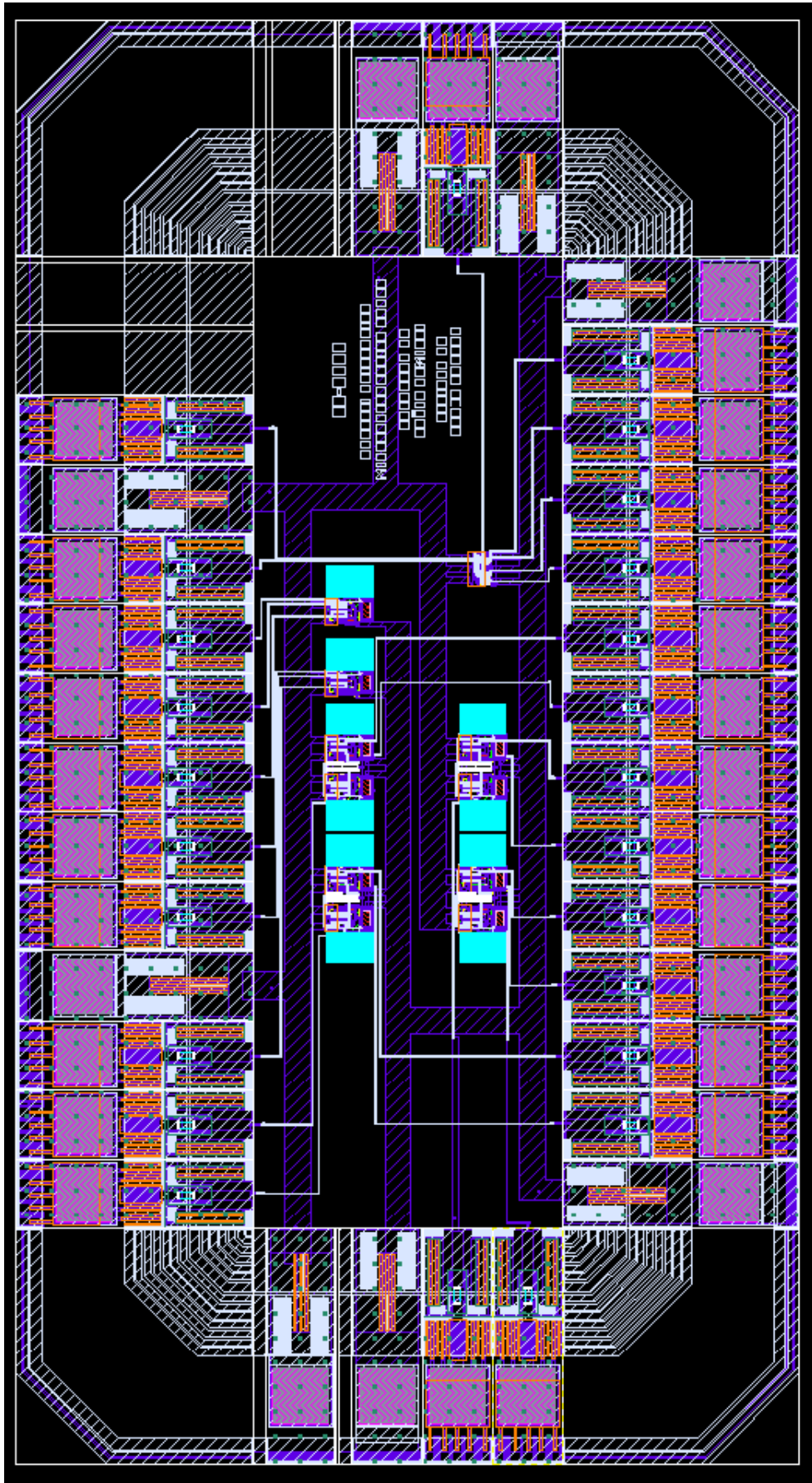


Figure C.2: Mask layout of operational transconductance amplifier

Bibliography

BIBLIOGRAPHY

- [1] C. Hagleitner, A. Schaufelbuhl, O. Brand, H. Baltes, C. Menolfi, and Q. Huang, "Micro-machined CMOS calorimetric chemical sensor with on-chip low noise amplifier", Proc. IEEE Workshop on Micro Electro Mechanical Systems MEMS 99, Orlando, 1999
- [2] Y. S. Lee and K. D. Wise, "A batch-fabricated silicon capacitive pressure transducers with low temperature sensitivity", IEEE Transactions on Electron Devices, vol. ED-29, no. 1, Jan 1982, pp. 42-48.
- [3] <http://www.analog.com/imems/>
- [4] An SPC Market Study - January 1999, Microelectromechanical Systems (MEMS): Emerging Applications and Markets (Mr. Bill Detlefs, System Planning Corporation)
- [5] N. Taguchi, Japanese Patent 45-38200
- [6] N. Taguchi, Japanese Patent 47-38840
- [7] N. Taguchi, US Patent 3 644 795
- [8] A. Arbab, A. Spetz, Q. U. Wahab, M. Willander, and I. Lunstrom, "Chemical sensors for high temperatures based on silicon carbide", Sensors Mater, 4 (1993) 173-185
- [9] W. P. Kang, Y. Gurbuz, J. L. Davidson and D. V. Kerns, "A new hydrogen sensor using a polycrystalline diamond-based schottky diode", J. Electrochemical Soc., 141 (1994)
- [10] Y. Gurbuz, W. P. Kang, J. L. Davidson, and D. V. Kerns, "Analysis of Current Conduction Mechanism and Gas Adsorption Effects on Device Parameters of Diamond Based Oxygen Gas Sensor", IEEE Transactions on Electron Devices Volume 46, Issue 5, 1999, Pages 914-920 2231-2234

- [11] J.B.W.H. Brattain, "Surface properties of germanium", *Bell. Syst. Tech. J.* 32 (1952) 1.
- [12] T. Seiyama, A. Kato, K. Fujushi, M. Nagatani, "A new detector for gaseous components using semiconductive thin films", *Anal. Chem.* 34 (1962) 1502f.
- [13] W. Gopel, K. Schierbaum, "SnO₂ sensors: current status and future prospects", *Sensors & Actuators B* 26/27 (1995) 1-12
- [14] P. Hauptman, "Sensor-Principles and Applications, Carl Hanser Verlag & Prentice Hall), 1993,115-153.
- [15] J.W. Gardner, "Microsensors-Principles and Applications", John-Wiley & Sons, 1994, 224-246
- [16] J.W. Gardner and P.N. Barlet, "Electronic Noses-Principles and Applications", Oxford, 1999, 67-100
- [17] D. Diamond, "Principles of Chemical and Biological Sensors", John-Wiley & Sons, 1998, 236-240
- [18] G.Z..Sauerbrey, *Z. Phys.*, 1959,155,206-222
- [19] C.G. Fox and J.F. Alder, "Techniques and mechanisms in gas sensing", ed. by P.T.Mosely, I.O.W. Norries and D.E. Williams, Adam Hilger, Bristol, 1991, 324-346
- [20] J.W. Grate, S.J.Martin and R.M.White, *Anal.Chem.*,1993,65,940-948
- [21] J.W.Grata, S.J.Martin and R.M.White, *Anal. Chem.*, 1993, 65, 987-996
- [22] B. Liedberg, C. Nylander and I. Lundstrom, *Sensors & Actuators*, 1983, 4, 299-302
- [23] E. Kretchmann, *Z. Phys.*, 1971.241,313
- [24] K. S. Johnston, S. R. Karlson, C. Jung and S. S. Yee, *Mater. Chem. Phys.*, 1995, 42-242
- [25] B. Chadwick and M. Gal., *Jpn. J. Appl. Phys.*, 1993, 32, 2716
- [26] S. Nelson, K. S. Johnston and S.S. Yee, *Sensors & Actuators*, 1996, B35/36, 187

- [27] H. Nanto, M. Habara, N. Dougami, T. Mukai, H. Sugiyama, E. Kusano, A. Kinbara and Y. Douguchi, Tech. Digest of the 7th Inter. Meeting on Chemical Sensors, 1998, 695-697
- [28] T. Seiyama, A. Kato, K. Fullishi, M. Nagatani, Anal. Chem. 34, 1962, 1502
- [29] I. Lundstrom, S. Shivaraman, C. Svensson and L. Lundkuist, Appl. Phys. Lett., 1975, 26, 55-57
- [30] I. Lundstrom, E. Hedborg, A. Spetz, . Sundgren and F. Winquist, Sensors and Sensory Sistems for an Electronic Nose (ed. J. W. Gardner and P.N.Barlett), NATOASI Series (Kluwer, Dordrecht), 1992, 212, 303-319
- [31] ANSYS is a registered trademark of Swanson Analysis System Inc.
- [32] C.O. Bennett, J.E. Myers, "Momentum, Heat and Mass Transfer", McGraw-Hill International Editions, Chemical Engineering Series
- [33] J.P. Holman, "Heat Transfer", Mc-Graw Hill, 1996
- [34] I. Simon, N. Bârsan, M. Bauer, U. Weimar, "Micormachined metal oxide gas sensors: opportunities to improve sensor performance", Sensors & Actuators B, 73, 2001, 1-26
- [35] C. Mastrangelo, W. Tang, Semiconductor sensor technologies, in:S. Sze(Ed.), Semiconductor Sensors, Wiley, 1994, Chapter 2, pp. 17-95.
- [36] C. Rossi, P.T. Boyer, D. Esteve, Sensors and Actuators A 64 (1998) 147-150
- [37] R. F. Wassenaar, Mohammed Ismail, Chi-Hung Lin, "Operational Transconductance Amplifier", The VLSI Handbook, (Dd. by Wai Kai Chen), CRC Press & IEEE Press
- [38] D. Leblebici, "Some comments on Basic Current Mirros and Application to OTA"
- [39] G. Meckel, "CAD models of MSFETS", F. Van de Wiele, W. L. Engl, P.G. Jespers(editors), Noordhoff,1977.
- [40] Austria Micro Systems
- [41] Cadence Design Framework

BIBLIOGRAPHY

- [1] C. Hagleitner, A. Schaufelbuhl, O. Brand, H. Baltes, C. Menolfi, and Q. Huang, "Micro-machined CMOS calorimetric chemical sensor with on-chip low noise amplifier", Proc. IEEE Workshop on Micro Electro Mechanical Systems MEMS 99, Orlando, 1999
- [2] Y. S. Lee and K. D. Wise, "A batch-fabricated silicon capacitive pressure transducers with low temperature sensitivity", IEEE Transactions on Electron Devices, vol. ED-29, no. 1, Jan 1982, pp. 42-48.
- [3] <http://www.analog.com/imems/>
- [4] An SPC Market Study - January 1999, Microelectromechanical Systems (MEMS): Emerging Applications and Markets (Mr. Bill Detlefs, System Planning Corporation)
- [5] N. Taguchi, Japanese Patent 45-38200
- [6] N. Taguchi, Japanese Patent 47-38840
- [7] N. Taguchi, US Patent 3 644 795
- [8] A. Arbab, A. Spetz, Q. U. Wahab, M. Willander, and I. Lunstrom, "Chemical sensors for high temperatures based on silicon carbide", Sensors Mater, 4 (1993) 173-185
- [9] W. P. Kang, Y. Gurbuz, J. L. Davidson and D. V. Kerns, "A new hydrogen sensor using a polycrystalline diamond-based schottky diode", J. Electrochemical Soc., 141 (1994)
- [10] Y. Gurbuz, W. P. Kang, J. L. Davidson, and D. V. Kerns, "Analysis of Current Conduction Mechanism and Gas Adsorption Effects on Device Parameters of Diamond Based Oxygen Gas Sensor", IEEE Transactions on Electron Devices Volume 46, Issue 5, 1999, Pages 914-920 2231-2234

- [11] J.B.W.H. Brattain, "Surface properties of germanium", *Bell. Syst. Tech. J.* 32 (1952) 1.
- [12] T. Seiyama, A. Kato, K. Fujushi, M. Nagatani, "A new detector for gaseous components using semiconductive thin films", *Anal. Chem.* 34 (1962) 1502f.
- [13] W. Gopel, K. Schierbaum, "SnO₂ sensors: current status and future prospects", *Sensors & Actuators B* 26/27 (1995) 1-12
- [14] P. Hauptman, "Sensor-Principles and Applications, Carl Hanser Verlag & Prentice Hall), 1993,115-153.
- [15] J.W. Gardner, "Microsensors-Principles and Applications", John-Wiley & Sons, 1994, 224-246
- [16] J.W. Gardner and P.N. Barlet, "Electronic Noses-Principles and Applications", Oxford, 1999, 67-100
- [17] D. Diamond, "Principles of Chemical and Biological Sensors", John-Wiley & Sons, 1998, 236-240
- [18] G.Z..Sauerbrey, *Z, Phys.*, 1959,155,206-222
- [19] C.G. Fox and J.F. Alder, "Techniques and mechanisms in gas sensing", ed. by P.T.Mosely, I.O.W. Norries and D.E. Williams, Adam Hilger, Bristol, 1991, 324-346
- [20] J.W. Grate, S.J.Martin and R.M.White, *Anal.Chem*,1993,65,940-948
- [21] J.W.Grate, S.J.Martin and R.M.White, *Anal. Chem*, 1993, 65, 987-996
- [22] B. Liedberg, C. Nylander and I. Lundstrom, *Sensors & Actuators*, 1983, 4, 299-302
- [23] E. Kretchmann, *Z. Phys.*, 1971.241,313
- [24] K. S. Johnston, S. R. Karlson, C. Jung and S. S. Yee, *Mater. Chem. Phys.*, 1995, 42-242
- [25] B. Chadwick and M. Gal., *Jpn. J. Appl. Phys.*, 1993, 32, 2716
- [26] S. Nelson, K. S. Johnston and S.S. Yee, *Sensors & Actuators*, 1996, B35/36, 187

- [27] H. Nanto, M. Habara, N. Dougami, T. Mukai, H. Sugiyama, E. Kusano, A. Kinbara and Y. Douguchi, Tech. Digest of the 7th Inter. Meeting on Chemical Sensors, 1998, 695-697
- [28] T. Seiyama, A. Kato, K. Fullishi, M. Nagatani, Anal. Chem. 34, 1962, 1502
- [29] I. Lundstrom, S. Shivaraman, C. Svensson and L. Lundkuist, Appl. Phys. Lett., 1975, 26, 55-57
- [30] I. Lundstrom, E. Hedborg, A. Spetz, . Sundgren and F. Winquist, Sensors and Sensory Sistems for an Electronic Nose (ed. J. W. Gardner and P.N.Barlett), NATOASI Series (Kluwer, Dordrecht), 1992, 212, 303-319
- [31] ANSYS is a registered trademark of Swanson Analysis System Inc.
- [32] C.O. Bennett, J.E. Myers, "Momentum, Heat and Mass Transfer", McGraw-Hill International Editions, Chemical Engineering Series
- [33] J.P. Holman, "Heat Transfer", Mc-Graw Hill, 1996
- [34] I. Simon, N. Bârsan, M. Bauer, U. Weimar, "Micormachined metal oxide gas sensors: opportunities to improve sensor performance", Sensors & Actuators B, 73, 2001, 1-26
- [35] C. Mastrangelo, W. Tang, Semiconductor sensor technologies, in:S. Sze(Ed.), Semiconductor Sensors, Wiley, 1994, Chapter 2, pp. 17-95.
- [36] C. Rossi, P.T. Boyer, D. Esteve, Sensors and Actuators A 64 (1998) 147-150
- [37] R. F. Wassenaar, Mohammed Ismail, Chi-Hung Lin, "Operational Transconductance Amplifier", The VLSI Handbook, (Dd. by Wai Kai Chen), CRC Press & IEEE Press
- [38] D. Leblebici, "Some comments on Basic Current Mirros and Application to OTA"
- [39] G. Meckel, "CAD models of MSFETS", F. Van de Wiele, W. L. Engl, P.G. Jespers(editors), Noordhoff,1977.
- [40] Austria Micro Systems
- [41] Cadence Design Framework